DISSERTATIONS IN
FORESTRY AND
NATURAL SCIENCES

Dong Liu

Non-linear Difference Imaging Approach to Electrical Impedance Tomography

Publications of the University of Eastern Finland
Dissertations in Forestry and Natural Sciences No 206

UNIVERSITY OF
EASTERN FINLAND

DONG LIU

Non-linear Difference Imaging Approach to Electrical Impedance Tomography

Publications of the University of Eastern Finland
Dissertations in Forestry and Natural Sciences
No 206

Academic Dissertation
To be presented by permission of the Faculty of Science and Forestry for public examination in the Auditorium SN201 in Snellmania Building at the University of Eastern Finland, Kuopio, on December, 12, 2015,
at 12 o'clock noon.

Department of Applied Physics

Grano Oy
Jyväskylä, 2015
Editor: Prof. Pertti Pasanen,
Prof. Kai Peiponen, Prof. Matti Vornanen, Prof. Pekka Kilpelainen

Distribution:
University of Eastern Finland Library / Sales of publications
P.O.Box 107, FI-80101 Joensuu, Finland
tel. +358-50-3058396
`http://www.uef.fi/kirjasto`

ISBN: 978-952-61-1994-6 (printed)
ISBN: 978-952-61-1995-3 (pdf)
ISSNL: 1798-5668
ISSN: 1798-5668
ISSN: 1798-5676 (pdf)

Author's address:
University of Eastern Finland
Department of Applied Physics
P.O.Box 1627
FI-70211 Kuopio, Finland
email: `dong.liu@uef.fi`

Supervisors:
Docent Aku Seppänen, PhD
University of Eastern Finland
Department of Applied Physics
Kuopio, Finland
email: `aku.seppanen@uef.fi`

Associate Professor Ville Kolehmainen, PhD
University of Eastern Finland
Department of Applied Physics
Kuopio, Finland
email: `ville.kolehmainen@uef.fi`

Professor Samuli Siltanen, PhD
University of Helsinki
Department of Mathematics and Statistics
Helsinki, Finland
email: `samuli.siltanen@helsinki.fi`

Professor Anne-Maria Laukkanen, PhD
University of Tampere
School of Education
Tampere, Finland
email: `anne-maria.laukkanen@uta.fi`

Reviewers:
Associate Professor Kim Knudsen, PhD
Technical University of Denmark
Department of Mathematics and
Computer Science
Kgs. Lyngby, Denmark
email: `kiknu@dtu.dk`

Professor Bastian von Harrach, PhD
Goethe University
Institute of Mathematics
Frankfurt, Germany
email: `harrach@math.uni-frankfurt.de`

Opponent:
Assistant Professor Mohammad Pour-Ghaz, PhD
North Carolina State University
Department of Civil, Construction, and
Environmental Engineering
Box 7908, Raleigh, NC 27695
North Carolina, USA
email: `mpourgh@ncsu.edu`

ABSTRACT

In electrical impedance tomography (EIT), electrical currents are injected into an object using a set of electrodes attached on the surface of the object and the resulting electrode potentials are measured. The conductivity of the object is reconstructed as a spatially distributed parameter based on the known currents and measured potentials. The EIT image reconstruction problem is an *ill-posed* inverse problem. That is, the solution is highly intolerant of measurement noise and modeling errors, arising from model reductions and inaccurate knowledge of auxiliary model parameters such as electrode positions, contact impedances and boundary shape of the body. Therefore, the EIT reconstruction requires accurate modeling of the measurements and tailored inversion methods.

In many applications of EIT, the goal is to reconstruct a change in the conductivity between two states measured at different times or frequencies. This mode of EIT is usually referred to as *difference imaging*. The image reconstruction in difference imaging is conventionally carried out using a linear approach, where the conductivity change is reconstructed based on the difference of the measurements and a global linearization of the non-linear forward problem. One of the main reasons for its popularity is that the linear approach tolerates modeling errors to an extent. However, the linear approach is highly approximative since the actual non-linear forward mapping is approximated by a linear one. Consequently, the images are often only qualitative in nature and their spatial resolution can be weak.

In this thesis, a novel non-linear difference imaging approach to reconstruct changes in a target conductivity from EIT measurements is developed. The key feature of the approach is that the conductivity after the change is parameterized as a linear combination of the (unknown) initial state and the conductivity change. This allows for modeling independently the spatial properties of the background conductivity and the conductivity change by separate regularization functionals. The approach also allows in a straightforward way to restrict the conductivity change to a localized region of interest inside the domain.

The performance of the proposed method is tested with simulated and experimental 2D and 3D EIT data, and is compared against the conventional linearized reconstruction and separate absolute reconstructions. Since the conventional linear approach to difference imaging has good tolerance for modeling errors, we study to which extent does the non-linear approach tolerate modeling errors. The results show that the non-linear approach combines the advantages of absolute and difference imaging, and tolerates modeling errors at least to the same extent as the conventional linear approach, producing quantitative information on the conductivity change. In addition, we also investigate the effect of infeasible choices for regularization functionals in the non-linear approach.

Universal Decimal Classification: 519.6, 537.31, 621.3.011.2, 621.317.33

National Library of Medicine Classification: WN 206, QT 36, WG 141.5.T6

INSPEC Thesaurus: imaging; image reconstruction; difference imaging; tomography; electrical impedance tomography; inverse problems; modeling errors; measurement errors; electrical conductivity; non-linear systems

Yleinen suomalainen asiasanasto: kuvantaminen; tomografia; impedanssitomografia; virheet; mallinnusvirheet; mittausvirheet; sähkönjohtavuus;

Acknowledgments

This study was carried out in the Department of Applied Physics at the University of Eastern Finland during the years 2011-2015.

I am very grateful to my main supervisor Docent Aku Seppänen, PhD, and Associate Professor Ville Kolehmainen, PhD, for their valuable guidance and encouragement during the years. I also want to thank my other supervisors Professor Samuli Siltanen, PhD, and Professor Anne-Maria Laukkanen, PhD, for their guidance and fruitful discussions, and for giving the opportunity to work in the Computational Science Research Programme of the Academy of Finland (LASTU). In addition, I thank Professor Jari P. Kaipio, PhD, for originally employing me.

I want to give my best thanks to the official reviewers Associate Professor Kim Knudsen, PhD, and Professor Bastian von Harrach, PhD, for the assessment of the thesis.

I am honored and looking forward to having Assistant Professor Mohammad Pour-Ghaz, PhD, as my dissertation opponent.

I also greatly appreciate Professor Raul Gonzalez Lima, PhD, from the Department of Mechanical Engineering, University of São Paulo, for having the opportunity to visit his excellent EIT Laboratory. I want to express my gratitude to Erick León, PhD and Fernando Moura, PhD, from the Department of Mechanical Engineering, University of São Paulo, for their help with 3D mesh generator.

I wish to thank the staff of the Department of Applied Physics for their support. I would like to thank Tuomo Savolainen, PhD, and Paula Kaipio, for the assistance with EIT laboratory measurements. I thank all my colleagues in the Inverse Problems group for the support and for the pleasant working atmosphere. Especially, I thank Antti Nissinen, PhD, Antti Lipponen, PhD, Gerardo del Muro Gonzalez, M.Sc, and Meghdoot Mozumder, M.Sc for their friendship, support and for academic and non-academic discussions.

Finally, my deepest gratitude and loving appreciation go to my mother Lanxiu Zhu and my brother Jun Liu, PhD, who have supported and encouraged me with unconditional love and dedication, especially during difficult moments. Unfathomable gratitude of mine is for my fiancee Weijia Li, who always helped me stay the course. Without their devotion, I may not have completed my PhD study. I dedicate this thesis to the memory of my beloved father, Mr. Yanxiong Liu (1954-2012), whom I lost during my stay in Finland. My father was a talented design engineer, whose loving and dignified presence I truly miss.

Appreciatively, this thesis was financially supported by the Academy of Finland, Finnish Centre of Excellent (CoE) in Inverse Problems Research 2006-2011 and 2012-2017, the Finnish Doctoral Programme in Computational Sciences (FICS), and the Doctoral program in mathematical analysis and scientific computing of the University of Eastern Finland.

Kuopio, November 25, 2015 *Dong Liu*

LIST OF PUBLICATIONS

This thesis consists of an overview and the following three original articles which are referred to in the text by their Roman numerals **I-III**.

I D. Liu, V. Kolehmainen, S. Siltanen, A.M. Laukkanen and A. Seppänen, "Estimation of conductivity changes in a region of interest with electrical impedance tomography," *Inverse Problems and Imaging* **9,** 211–229, 2015.

II D. Liu, V. Kolehmainen, S. Siltanen and A. Seppänen, "A nonlinear approach to difference imaging in EIT; assessment of the robustness in the presence of modelling errors," *Inverse Problems* **31,** 035012, 2015.

III D. Liu, V. Kolehmainen, S. Siltanen, A.M. Laukkanen and A. Seppänen, "Non-linear difference imaging approach to three-dimensional electrical impedance tomography in the presence of geometric modeling errors," In Review *IEEE Transactions on Biomedical Engineering*, 2015.

The original articles have been reproduced with permission of the copyright holders.

AUTHOR'S CONTRIBUTION

All publications are results of joint work with the supervisors and co-authors. The author wrote Publications **I-III** in co-operation with supervisors. The author implemented all the numerical computations using Matlab® and computed all the results in Publications **I-III**. The finite element method codes used for the forward solution of the EIT problem have been previously developed in the Inverse Problems group in the Department of Applied Physics. The author conducted the measurements in Publications **I-III** in collaboration with the EIT laboratory staff.

Contents

1 Introduction

Electrical impedance tomography (EIT) is an imaging modality in which the conductivity distribution of a body is estimated from measurements of electrical currents and electrode potentials at the boundary of the body [1–3]. EIT has applications in geophysical exploration [4,5], underwater applications [6–9], biomedical imaging [10–15], industrial process monitoring and control [16–18], and non-destructive testing [19–24]. For reviews of EIT, see [2,3,25–27].

The image reconstruction problem in EIT is an *ill-posed* inverse problem, which makes the solution highly intolerant to modeling errors. Therefore, to obtain a feasible estimate of the conductivity distribution, appropriate reconstruction methods have to be chosen.

Methods for EIT imaging can be categorized as *absolute imaging* [12,28] and *difference imaging* [3,14,15,29–34]. In absolute imaging, the conductivity distribution is reconstructed based on potential measurements corresponding to a single instant of time. To produce a feasible absolute image, the auxiliary model parameters, such as the boundary shape of the target body, contact impedances and electrode positions, need to be known accurately. However, this information is usually inaccurately known. It has been shown that errors in modeling of the auxiliary parameters (e.g. boundary shape), can lead to severe errors in the reconstruction [35,36].

On the other hand, in difference imaging, the conductivity change is reconstructed based on data sets measured before and after the conductivity change. For example, in the lung imaging, the data before the change might be measured at respiratory expiration and the data after the change at inspiration, in such a way that the difference image shows the conductivity change between expiration and inspiration [3,10,37]. In the conventional linear approach to difference imaging, the non-linear mapping between the electrical conductivity and the electrode potentials is approximated by a global linearization and taking difference of the data sets, the reconstruction becomes a linear problem. The linear problem can be solved, for example, by regularized linear least squares (LS) problem. The linear approach to difference imaging has been shown to preserve the inclusion shape and position of the conductivity change in the continuum limit [38]. We note, however, that in a realistic EIT setting with a limited number of electrodes and with measurement errors, the solutions need to be regularized, and the quality of the reconstruction depends heavily on the chosen regularization [39]. The linear difference reconstruction has also been found to tolerate modeling errors to an extent. This feature occurs when the unknown auxiliary model parameters (e.g. boundary shape or contact impedances) are invariant between the measurement states, leading to partial cancellation of the modeling errors when the difference of the measurements is computed.

Although the linear approach to difference imaging is able to suppress some of the effects of modeling errors, it has been shown that artefacts are still present in the reconstructions [40–42]. Furthermore, a drawback of the linear approach is that the linear approximation for the non-linear forward model is only feasible for small deviations from the initial conductivity [43]. In high contrast cases, for example in imaging of accumulation of well conducting liquid (haematothorax) or poorly conducting air (pneumothorax) in the lungs, the linear approach may be insufficient for detecting clinically relevant information in the lung [44]. Moreover, the performance depends on the linearization point which should ideally be equal to the initial state, which is usually unknown. Conventionally, the linearization point is selected as a homogeneous estimate of the conductivity of the initial state. However, in practical medical applications, the initial state is often highly inhomogeneous. Due to these problems, difference imaging with linear approach usually only provides qualitative information on the conductivity change.

To achieve quantitative information of the conductivity change, it would be preferable to use a non-linear model in the solution of the difference imaging, and to model independently the background and the conductivity change, which may exhibit different spatial characteristics. Furthermore, in some applications, the conductivity change is often known to occur in a region of interest (ROI) inside the body. Utilizing this information could improve the quality of the reconstruction. Examples of such applications are monitoring of water ingress in soil [4] and cracking of concrete [20, 22, 23], underwater object tracking [45], assessment of regional lung ventilation [46–50], monitoring of cardiac stroke [51] and intra-peritoneal bleeding [52]. This is also the case in a potential new application of EIT: imaging of vocal folds in voice loading studies [53–56]. Indeed, the location of the glottis is known relatively well, and vocal folds are the most rapidly moving part in a human body; hence, during the movement of vocal folds, the conductivity changes outside a relatively small volume around the glottis are negligible.

In this thesis, a non-linear reconstruction method for difference imaging is proposed. The new method presented in Publication **I** is based on the regularized non-linear LS framework. The EIT measurements before and after the change are concatenated into a single measurement vector and two images corresponding to the initial conductivity and the conductivity change are simultaneously reconstructed based on the combined data. The key feature of this approach is that the conductivity after the change is parameterized as a linear combination of the (unknown) initial state and the conductivity change. Therefore, it naturally allows for modeling independently the spatial characteristics of the initial conductivity (background) and the conductivity change, by using different regularization functionals. The approach also allows in a straightforward way to restrict the conductivity change to a subvolume when the conductivity change is known to occur in some specific ROI inside the body.

Finally, we note that the non-linear difference imaging approach developed in this thesis is not confined to EIT only and the extensions to other imaging modalities are mostly straightforward. Recently, the non-linear difference imaging has successfully been applied to optical tomography [57].

Aims and contents of this thesis

The thesis consists of three publications. The aim and content of each study are:

1. To develop a novel non-linear difference imaging approach for reconstruction of changes in a target conductivity from EIT measurements. The proposed approach is evaluated both with simulated measurements in a computed tomography scan based human neck geometry and with experimental measurements from a water tank phantom. (**I**)

2. To study the robustness of the non-linear difference imaging approach with respect to modeling errors due to domain truncation, unknown contact impedances, inaccurately known electrode positions and inaccurately known domain boundary. The non-linear difference imaging approach is evaluated with numerical and experimental data. (**II**)

3. To investigate the applicability of the non-linear difference imaging approach for three-dimensional (3D) EIT in the presence of geometric modeling errors. The feasibility of the approach is evaluated with simulated examples of glottal imaging, cardiac imaging and lung imaging, and also with experimental data from a laboratory setting. (**III**)

This thesis is organized as follows. In Chapter 2, the forward model and notations in EIT are described. The reconstruction problem and modeling errors in EIT are also reviewed briefly in Chapter 2. The non-linear difference imaging approach in EIT is proposed in Chapter 3. In addition, potential applications of non-linear difference imaging are briefly outlined in Chapter 3. The review of the results is given in Chapter 4. Some unpublished results of a study of the effect of infeasible choices for regularization functionals in the non-linear approach are also presented in Chapter 4. In Chapter 5, summary and conclusions of the thesis are given.

2 Electrical Impedance Tomography

In Section 2.1, the forward problem of EIT is explained. The forward model describes how the electrode potentials can be determined when the conductivity of the object and the injected currents are known. In this thesis, the so-called complete electrode model (CEM) is used as the forward model. The solution of the forward problem is approximated by finite element (FE) method. The FE approximation of the CEM and the measurement noise model are also described in Section 2.1. Section 2.2, briefly reviews the inverse problems in EIT. The discussion is concentrated on the sources of modeling errors, and reconstruction methods. For reviews on EIT, see for example [2, 3, 26, 27].

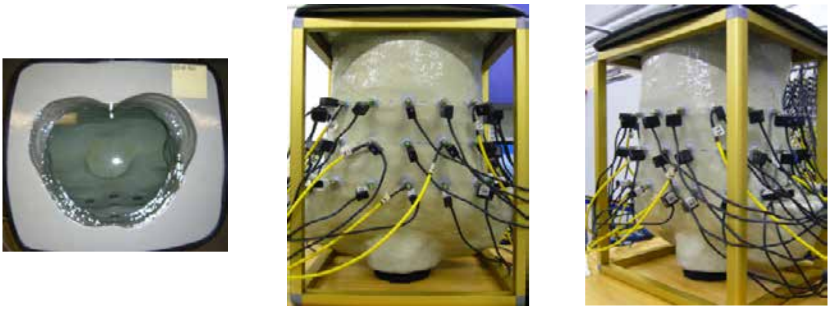

Figure 2.1: A thorax-shaped measurement tank used in Publication **III**. *Left to right: views from the top, front and side, respectively.*

2.1 FORWARD MODEL AND NOTATION

In EIT, L contact electrodes e_ℓ are attached to the boundary of the body, see Figure 2.1. A set of electric currents is injected into the body through these electrodes, and the resulting potentials are measured using the same electrodes. Based on the electrode potentials and known currents, the internal conductivity distribution of the object is estimated.

To solve the reconstruction problem one needs to solve the forward problem for some assumed conductivity so that the predicted potentials can be compared with the measured data. We model the EIT measurements with the CEM [1], which consists of the following partial differential equation and the boundary conditions:

$$\begin{aligned}
\nabla \cdot (\sigma(x)\nabla u(x)) &= 0\,,\ x \in \Omega && (2.1)\\
u(x) + z_\ell \sigma(x)\frac{\partial u(x)}{\partial n} &= U_\ell,\ x \in e_\ell,\ \ell = 1, ..., L && (2.2)\\
\int_{e_\ell} \sigma(x)\frac{\partial u(x)}{\partial n}\,\mathrm{d}S &= I_\ell,\ \ \ell = 1, ..., L && (2.3)\\
\sigma(x)\frac{\partial u(x)}{\partial n} &= 0,\ \ x \in \partial\Omega \backslash \bigcup_{\ell=1}^{L} e_\ell, && (2.4)
\end{aligned}$$

where $\sigma(x)$ is the conductivity, $u(x)$ is the electric potential distribution inside the target domain Ω, $x \in \Omega$ is the spatial coordinate, and n denotes the outward unit normal vector on the boundary $\partial\Omega$. Contact impedances, electrode potentials, and injected currents corresponding to the electrodes e_ℓ are denoted by z_ℓ, U_ℓ and I_ℓ, respectively. The currents satisfy the charge conservation law

$$\sum_{\ell=1}^{L} I_\ell = 0, \tag{2.5}$$

and a ground level for the potentials can be fixed for example by setting

$$\sum_{\ell=1}^{L} U_\ell = 0. \tag{2.6}$$

2.1.1 Finite element approximation of the forward model

The numerical solution of the model (2.1-2.6) is based on the FE approximation [28]. In the FE approximation, we write finite dimensional approximation

$$u(x) \quad = \quad \sum_{j=1}^{N_u} \alpha_j \psi_j(x), \tag{2.7}$$

for the potential $u(x)$ in the variational form of (2.1-2.6). Here N_u is the number of nodes in the FE mesh that is used for the representation of $u(x)$, and the functions $\psi_j(x)$ are the nodal basis functions of the FE mesh. In this study, the conductivity $\sigma(x)$ is approximated in a basis

$$\sigma(x) \quad = \quad \sum_{k=1}^{N_\sigma} \sigma_k \phi_k(x). \tag{2.8}$$

Typically, N_σ is the number of nodes in the FE mesh for the representation of $\sigma(x)$, and $\phi_k(x)$ are the nodal basis functions.

Then, using a standard Galerkin discretization, the solution of the forward problem becomes equivalent to solving a system of linear equations. In the following, we denote the discretized forward mapping

$$\sigma \mapsto U(\sigma)$$

by $U(\sigma)$. For details of the FE approximation, see [28,58].

2.1.2 Conventional noise model

The measurement noise in EIT is usually modeled as Gaussian additive noise which is mutually independent with the unknown conductivity, leading to the *observation model*:

$$V = U(\sigma) + e \tag{2.9}$$

where $V \in \mathbb{R}^M$ is the vector including all the measured electrode potentials , $M = mN_{\text{inj}}$. Here N_{inj} denotes the number of current injections and m is the number of measured potentials for each current injection. Moreover, $e \in \mathbb{R}^M$ is the Gaussian distributed measurement noise $e \sim \mathcal{N}(e^*, \Gamma_e)$. The mean $e^* \in \mathbb{R}^M$ and the covariance matrix $\Gamma_e \in \mathbb{R}^{M \times M}$ are usually estimated experimentally, see [59]. Note that the additive noise model is not always adequate. For example, measurement noise due to the disturbances in industry (e.g. power supply) can have various different noise characteristics. For this reason, more complicated noise models in inverse problems are discussed in [60].

2.2 INVERSE PROBLEM IN EIT

In this section, a brief review of modeling errors and the inversion methods in EIT is given. For a more comprehensive discussion on reconstruction methods in EIT, see [25, 61–63].

2.2.1 Modeling errors in EIT

The *ill-posed* nature of the EIT reconstruction problem means that the problem is highly intolerant to measurement noise and modeling errors. The effect of the measurement noise can often be reduced by using an accurate measurement system and by careful modeling of the measurement error statistics.

Modeling errors, on the other hand, are often related to model reductions, such as truncation of the computational domain, and inaccurate knowledge of auxiliary model parameters such as the contact impedances, electrode positions and boundary of the target body. For example, the computational domain has to be often truncated because of limited computational resources and time. One such application is EIT monitoring of industrial processes, where the truncated models of flow pipes have to be often used. As another example, consider EIT monitoring of the pulmonary function. In practice, the shape of the thorax varies due to breathing and changes with the patient position during measurements. Therefore, the shape of the thorax and electrode positions are never known accurately.

A few approaches to absolute imaging (see Section 2.2.2) have been proposed to recover from the inaccurately known auxiliary parameters, e.g. for recovering from the inaccurately known boundary shape, a method based on anisotropic conductivities and Teichmüller spaces was introduced in [64–66]. Another way to coping with inaccurately known auxiliary parameters in the models is to consider them as unknown parameters in the image reconstruction. For example, simultaneous estimation of the conductivity and contact impedances has been considered in [59, 67]; the conductivity and boundary shape are simultaneously reconstructed in [68, 69]. Also in [70], the systematic errors induced by inaccurately known boundary shape and contact impedances are eliminated as part of the image reconstruction.

The so-called approximation error method (AEM) [60,71], based on the Bayesian framework, is an alternative for the above approaches. The key idea in the AEM is, loosely speaking, to represent not only the measurement noise, but also the errors due to inaccurate modeling of the target as an auxiliary noise process in the observation model. The statistics of the modeling errors are approximated via simulations based on prior distribution models for the conductivity and the auxiliary parameters. For a more extensive discussion on handling of modeling errors by the AEM in EIT, we refer to [72–74].

In addition, the so-called D-bar method, which is based on a constructive uniqueness proof for 2D EIT [75–77], has also been demonstrated to have some tolerance against domain modeling errors [78].

In difference imaging, the traditional way to circumvent the problems of modeling errors has been to use linearization-based reconstruction, which will be discussed in Section 2.2.3. The tolerance of the new non-linear difference imaging approach *w.r.t* modeling errors is discussed in Chapter 4 and Publications **II-III**.

2.2.2 Absolute imaging

In absolute imaging, the conductivity σ is reconstructed using a single set of potential measurements V during which the target is modeled to be non-varying. Most of the current approaches to the

EIT inverse problem are based on the regularized non-linear LS approach [79], that is, the conductivity is obtained as a solution of a minimization problem of the form

$$\hat{\sigma} = \arg\min_{\sigma>0}\{\|L_e(V - U(\sigma))\|^2 + p_\sigma(\sigma)\} \tag{2.10}$$

where L_e is a Cholesky factor of the noise precision matrix, i.e. $L_e^{\mathrm{T}}L_e = \Gamma_e^{-1}$, and $p_\sigma(\sigma)$ is a regularization functional. The functional $p_\sigma(\sigma)$ is usually designed such that it gives high penalty for unwanted/improbable features of σ.

The minimization problem (2.10) can be solved iteratively, for example with the Gauss-Newton method while the positivity constraint on the conductivity can be taken into account by using interior point methods [80,81]. For properties of different optimization methods in EIT, see e.g. [63].

Note that if the modeling errors are not taken into account, the solution of the non-linear absolute imaging problem can be highly erroneous, due to the ill-posedness of the inverse problem. This has been a major difficulty for realizations of practical applications of absolute imaging.

2.2.3 Linear difference imaging

In many applications of EIT, the goal is to monitor temporal changes in the conductivity. This is the case for example in functional medical imaging when the aim is to monitor blood volume changes in heart [82,83] or assess regional lung ventilation [46–50]. This mode of EIT is referred to as *difference imaging* [3,14,15,29–34] . Difference imaging is based on two EIT measurement realizations V_1 and V_2 at time instants t_1 and t_2, corresponding to conductivities σ_1 and σ_2, respectively. The observation models corresponding to the two EIT measurement realizations can be written as

$$V_1 = U(\sigma_1) + e_1 \tag{2.11}$$

$$V_2 = U(\sigma_2) + e_2 \tag{2.12}$$

where $e_i \sim \mathcal{N}(e^*, \Gamma_e),\ i = 1,2$.

In the conventional linear approach to difference imaging, models (2.11) and (2.12) are approximated by first order Taylor approximations as:

$$V_i \approx U(\sigma_0) + J(\sigma_i - \sigma_0) + e_i, \quad i = 1, 2 \tag{2.13}$$

where σ_0 is the linearization point, and $J = \frac{\partial U}{\partial \sigma}(\sigma_0)$ is the Jacobian matrix evaluated at σ_0. Using the linearizations and subtracting V_1 from V_2 gives the observation model

$$\delta V \approx J\delta\sigma + \delta e \tag{2.14}$$

where $\delta V = V_2 - V_1$, $\delta\sigma = \sigma_2 - \sigma_1$ and $\delta e = e_2 - e_1$.

Given the model (2.14), the objective in the linear difference imaging is to estimate the conductivity change $\delta\sigma$ based on the difference data δV. This leads to a minimization problem

$$\widehat{\delta\sigma} = \arg\min_{\delta\sigma}\{\|L_{\delta e}(\delta V - J\delta\sigma)\|^2 + p_{\delta\sigma}(\delta\sigma)\} \tag{2.15}$$

where $p_{\delta\sigma}(\delta\sigma)$ is a regularization functional. The weighting matrix $L_{\delta e}$ is defined as $L_{\delta e}^{\mathrm{T}} L_{\delta e} = \Gamma_{\delta e}^{-1}$, where $\Gamma_{\delta e}$, the covariance of the noise term δe is $\Gamma_{\delta e} = \Gamma_{e_1} + \Gamma_{e_2} = 2\Gamma_e$.

Note that the regularization functional $p_{\delta\sigma}(\delta\sigma)$ is often chosen to be of the quadratic form $p_{\delta\sigma}(\delta\sigma) = \|L_{\delta\sigma}\delta\sigma\|^2$ where $L_{\delta\sigma}$ is a regularization matrix. In such a case, (2.15) is of the form of a regularized linear LS problem, the solution of which can be computed with one step – in contrast to iterative solution of (2.10) in absolute imaging. The main benefit of the linear approach to difference imaging, however, is that when considering the difference data δV at least part of the systematic errors in the models/measurements are subtracted, and hence the estimates are often to some extent tolerant of systematic measurement and modeling errors. A drawback of the linear approach to difference imaging, however, is that the linear approximation for the non-linear observation model (2.9) is only feasible for small deviations from the initial conductivity [43], which can be insufficient for the detection of the clinically relevant high-contrast information [44]. Moreover, the performance depends on the selection of the linearization point σ_0 which should ideally be equal to the initial state, which is unknown. Conventionally, the initial state is approximated by a spatially constant conductivity which may be selected by a one-parameter LS fit to the data from the initial state. This choice can lead to significant errors in the reconstructions, especially if the background conductivity is highly inhomogeneous. Although the linear approach is known to reduce the reconstruction error due to modeling errors to some extent, it has been shown that artifacts are still present in the reconstructions [40–42]. To account for modeling errors caused by inaccurately known boundary shape and electrode positions, simultaneous reconstruction of the conductivity change and the electrode/boundary movements has been introduced to linear approach in difference imaging in [40, 42, 84]. However, these approaches have only been demonstrated to handle small conductivity changes and electrode/boundary movements.

3 Non-linear difference imaging in EIT

In Section 3.1, we describe a novel approach to EIT image reconstruction in cases where EIT measurements of a time-varying target are available before and after the change of the target. This approach is referred to as *non-linear difference imaging*. In the proposed approach, the conductivity after the change is represented as a linear combination of the initial conductivity and the conductivity change. Then, the initial conductivity and the conductivity change are reconstructed simultaneously, based on EIT data collected before and after the change of the target. The potential applications of non-linear difference imaging in EIT are briefly reviewed in Section 3.2.

3.1 NON-LINEAR DIFFERENCE IMAGING APPROACH

In principle, one could reconstruct the conductivities σ_1 and σ_2 by solving the minimization problem (2.10) *separately* for realizations V_i, $i = 1, 2$, and then estimate the conductivity change by $\delta\sigma = \sigma_2 - \sigma_1$. However, this approach is prone to the modeling errors [85]. The non-linear approach to difference imaging, on the other hand, aims at simultaneous reconstruction of the initial state σ_1 and the change $\delta\sigma$ based on measurements V_1 and V_2 and observation models (2.11) and (2.12).

In the non-linear difference imaging approach, conductivity σ_2 is modeled as a linear combination of the initial conductivity σ_1 and the change $\delta\sigma$. One feature of this parameterization is that it offers a straightforward way to restrict the conductivity change $\delta\sigma$ to a region of interest (ROI), if temporal changes are known to occur only in a subvolume inside the body. Let

$$\mathrm{supp}(\delta\sigma) = \Omega_{\mathrm{ROI}} \subseteq \Omega$$

denote the ROI, and denote the conductivity change within Ω_{ROI} by $\delta\sigma_{\mathrm{ROI}}$. Obviously, case $\Omega_{\mathrm{ROI}} = \Omega$ corresponds to the case where there are no subvolume constraints on the conductivity change. Then, we write

$$\delta\sigma = \mathcal{K}\delta\sigma_{\mathrm{ROI}},$$

where $\mathcal{K}$ is an extension mapping $\mathcal{K} : \Omega_{\mathrm{ROI}} \to \Omega$ such that

$$\mathcal{K}\delta\sigma_{\mathrm{ROI}} = \begin{cases} \delta\sigma_{\mathrm{ROI}} & x \in \Omega_{\mathrm{ROI}} \\ 0 & x \in \Omega \setminus \Omega_{\mathrm{ROI}} \end{cases} \tag{3.1}$$

and the conductivity σ_2 after the change is modeled as

$$\sigma_2 = \sigma_1 + \mathcal{K}\delta\sigma_{\mathrm{ROI}}. \tag{3.2}$$

Inserting model (3.2) to (2.12) and concatenating the measurement vectors V_1 and V_2 and the corresponding models in (2.11-2.12) into block vectors leads to the observation model

$$\underbrace{\begin{bmatrix} V_1 \\ V_2 \end{bmatrix}}_{\bar{V}} = \underbrace{\begin{bmatrix} U(\sigma_1) \\ U(\sigma_1 + \mathcal{K}\delta\sigma_{\mathrm{ROI}}) \end{bmatrix}}_{\bar{U}(\bar{\sigma})} + \underbrace{\begin{bmatrix} e_1 \\ e_2 \end{bmatrix}}_{\bar{e}} \tag{3.3}$$

or

$$\bar{V} = \bar{U}(\bar{\sigma}) + \bar{e}, \tag{3.4}$$

where

$$\bar{\sigma} = \begin{bmatrix} \sigma_1 \\ \delta\sigma_{\mathrm{ROI}} \end{bmatrix}.$$

Based on the observation model (3.4), the regularized LS solution to $\bar{\sigma}$ is obtained as

$$\hat{\bar{\sigma}} = \arg\min_{\bar{\sigma}} \{ \| L_{\bar{e}}(\bar{V} - \bar{U}(\bar{\sigma})) \|^2 + p_{\bar{\sigma}}(\bar{\sigma}) \}, \tag{3.5}$$

where $L_{\bar{e}} \in \mathbb{R}^{2M\times 2M}$ such that $L_{\bar{e}}^{\mathrm{T}} L_{\bar{e}} = \Gamma_{\bar{e}}^{-1}$ and

$$\Gamma_{\bar{e}} = \left[\begin{array}{cc} \Gamma_{e_1} & \mathbf{0}_{M\times M} \\ \mathbf{0}_{M\times M} & \Gamma_{e_2} \end{array} \right].$$

Typically, the noise statistics can be modeled as stationary, i.e., $\Gamma_{e_1} = \Gamma_{e_2} = \Gamma_e$. Further, the compound regularization functional $p_{\bar{\sigma}}(\bar{\sigma})$ is defined as

$$p_{\bar{\sigma}}(\bar{\sigma}) = p_{\sigma_1}(\sigma_1) + p_{\delta\sigma_{\mathrm{ROI}}}(\delta\sigma_{\mathrm{ROI}}), \tag{3.6}$$

which allows naturally designing different spatial models for σ_1 and $\delta\sigma$ to match different properties of the initial conductivity and the conductivity change. For example, $p_{\sigma_1}(\sigma_1)$ may correspond to the assumption of a smooth initial conductivity σ_1, while $p_{\delta\sigma_{\mathrm{ROI}}}(\delta\sigma_{\mathrm{ROI}})$ may correspond to a total variation (TV) model for the conductivity change.

The solution $\hat{\bar{\sigma}}$ of (3.5) has to be computed iteratively. In the iterations, the Jacobian matrix $J_{\bar{U}}(\bar{\sigma}) = \frac{\partial \bar{U}}{\partial \bar{\sigma}}$ is needed; the Jacobian is of the form

$$J_{\bar{U}}(\bar{\sigma}) = \left[\begin{array}{cc} J_U(\sigma_1) & \mathbf{0}_{M\times N_{\mathrm{ROI}}} \\ J_U(\sigma_1 + \mathcal{K}\delta\sigma_{\mathrm{ROI}}) & J_U(\sigma_1 + \mathcal{K}\delta\sigma_{\mathrm{ROI}})\mathcal{K} \end{array} \right]$$

where $J_U(\cdot)$ is the Jacobian matrix of the function $U(\cdot)$, $\mathbf{0}_{M\times N_{\mathrm{ROI}}} \in \mathbb{R}^{M\times N_{\mathrm{ROI}}}$ is an all-zero matrix, and N_{ROI} is the dimension of the vector $\delta\sigma_{\mathrm{ROI}}$.

In contrast to the conventional linear approach to difference imaging, the global linearization of the EIT forward model is *not* needed here, enabling the use of the two data realizations for quantitative imaging. Moreover, utilizing the information on the approximate position of the target change between the two measurement sets V_1 and V_2 is expected to improve the reconstructions, especially if the ROI is relatively small in comparison with the volume of the target.

In Publications **I-III** , the non-linear difference imaging approach is tested numerically and experimentally both in 2D and 3D studies.

The results are compared against the reconstructions of the conductivity change with the separate absolute reconstructions (Section 2.2.2) and the linear difference imaging approach (Section 2.2.3). Tolerance *w.r.t* various modeling errors is tested in Publications **II-III**. Modeling errors related to 1) truncation of the computational domain, 2) inaccurately known electrode positions, 3) unknown electrode contact impedances and 4) unknown exterior geometric shape are considered. For the results, see Chapter 4 and the Publications **I-III**.

3.2 POTENTIAL APPLICATIONS FOR NON-LINEAR DIFFERENCE IMAGING

There is a variety of potential applications for the non-linear difference imaging approach. As mentioned in Chapter 1, one application is the glottal imaging with EIT, especially imaging the vocal folds in voice loading studies [54–56, 86]. The measurements used in EIT are similar to the multi-channel-electroglottography system proposed in [53] for improving the assessment of glottal opening and the laryngeal position. The principle of that system is to register laryngeal behavior indirectly by measuring the change in electrical impedance across the throat during speaking. The results in [53] indicated that it is possible to track the location of glottis during a swallowing manoeuvre. However, the data was not used for image reconstruction. EIT could potentially serve as a tool for imaging the vocal folds movement during speech production. A nice property of the glottal imaging with EIT is the possibility of carrying out the reference measurements for difference imaging. Indeed, a test person can deliberately close or open the glottis for the reference measurements. Meanwhile, the location of the glottis is known relatively well, and vocal folds are the most rapidly moving part in a human body; hence, during the movement of vocal folds, the conductivity changes outside a relatively small volume around the glottis are negligible. Therefore, it is known *a priori* that the conductivity change can be restricted to a ROI subvolume inside the larynx, and the difference in the measured data is mainly due to a local change of the conductivity in the glottal area.

Another potential application for non-linear difference imaging approach lies in monitoring of the cardiac stroke, in which the heart is known to be located in the lower middle of the thoracic cavity, and the main interest is the conductivity change in the heart. Thus, the conductivity change is known *a priori* to be restricted to a ROI subvolume inside the thorax.

The other possible biomedical applications include, e.g. intraperitoneal bleeding [52] and assessment of regional lung ventilation [46–50]. Examples of possible geophysical applications are monitoring of water ingress in soil [4] and solute transport processes [87, 88]. The industrial applications include underwater object tracking [45], for example. The nondestructive testing applications include imaging of cracks in concrete [20,22,23], for example.

4 Review of the results

In this chapter, a brief review of the results of Publications **I-III** is given. Some unpublished results of a study of the effect of infeasible choices for regularization functionals in the non-linear approach are also shown in Section 4.3.3.

4.1 COMPUTED ESTIMATES

To study the performance of the non-linear difference imaging approach, the results are compared against the reconstructions of the conductivity change with absolute imaging and the linear difference imaging approach. The following estimates are computed in this thesis:

(E1) Absolute reconstructions of σ_1 and σ_2 by solving the minimization problem (2.10), leading to

$$\hat{\sigma}_i = \arg\min_{\sigma_i > 0}\{\|L_e(V_i - U(\sigma_i))\|^2 + \|L_\sigma(\sigma_i - \sigma^*)\|^2\},\ i = 1,2,$$

where V_i is the EIT measurement corresponding to the conductivity σ_i, $L_\sigma^{\mathrm{T}} L_\sigma = \Gamma_\sigma^{-1}$, and

$$\Gamma_\sigma(j,k) = a \exp\left\{-\frac{\|x_j - x_k\|_2^2}{2b^2}\right\} + c\delta_{jk}. \qquad (4.1)$$

Here, $\Gamma_\sigma(j,k)$ is the covariance matrix element (j,k) corresponding to the conductivities at the nodes in locations x_j and x_k [89]; a, b and c are positive scalar parameters, and δ_{jk} denotes the Kronecker delta function. Parameter a controls the variance of the nodal conductivity values, and parameter b controls the degree of spatial smoothness. The role of the term $c\delta_{jk}$ is to ensure that the covariance matrix is invertible. This choice of the regularization matrix L_σ is known to promote spatial smoothness to the estimates $\hat{\sigma}_i$. From these reconstructions, the estimate for the conductivity change is obtained by $\widehat{\delta\sigma} = \hat{\sigma}_2 - \hat{\sigma}_1$ [85].

(E2) **Linear difference reconstruction** of $\delta\sigma$ in the whole domain Ω by solving the minimization problem (2.15)

$$\widehat{\delta\sigma} = \arg\min_{\delta\sigma}\{\|L_{\delta e}(\delta V - J\delta\sigma)\|^2 + \|L_{\delta\sigma}\delta\sigma\|^2\}.$$

Here, $\delta V = V_2 - V_1$, J is the Jacobian matrix (see details in Section 2.2.3), and $L_{\delta\sigma}^{\mathrm{T}} L_{\delta\sigma} = \Gamma_{\delta\sigma}^{-1}$, where $\Gamma_{\delta\sigma}$ is constructed by equation (4.1).

(E3) **ROI constrained linear difference reconstruction** of $\delta\sigma_{\mathrm{ROI}}$ in the sub-domain Ω_{ROI} by solving

$$\begin{aligned}\widehat{\delta\sigma}_{\Omega_{\mathrm{ROI}}} = \arg \min_{\delta\sigma_{\Omega_{\mathrm{ROI}}}} \{&\|L_{\delta e}(\delta V - J_{\Omega_{\mathrm{ROI}}}\delta\sigma_{\Omega_{\mathrm{ROI}}})\|^2 \\ &+\|L_{\delta\sigma_{\Omega_{\mathrm{ROI}}}}\delta\sigma_{\Omega_{\mathrm{ROI}}}\|^2\}.\end{aligned}$$

Here, $J_{\Omega_{\mathrm{ROI}}} = J\mathcal{K}$, $\mathcal{K}$ is an extension mapping $\mathcal{K} : \Omega_{\mathrm{ROI}} \to \Omega$, $L_{\delta\sigma_{\Omega_{\mathrm{ROI}}}}^{\mathrm{T}} L_{\delta\sigma_{\Omega_{\mathrm{ROI}}}} = \Gamma_{\delta\sigma_{\Omega_{\mathrm{ROI}}}}^{-1}$ and $\Gamma_{\delta\sigma_{\Omega_{\mathrm{ROI}}}} = \mathcal{K}^{\mathrm{T}}\Gamma_{\delta\sigma}\mathcal{K}$. This estimate is computed as a reference of how the linear approach performs when a ROI constraint is employed.

(E4) Estimate of $\bar{\sigma} = (\sigma_1^{\mathrm{T}}, \delta\sigma_{\mathrm{ROI}}^{\mathrm{T}})^{\mathrm{T}}$ with the **ROI constrained non-linear difference reconstruction**.

$$\hat{\bar{\sigma}} = \arg\min_{\bar{\sigma}} \{\|L_{\bar{e}}(\bar{V} - \bar{U}(\bar{\sigma}))\|^2 + p_{\bar{\sigma}}(\bar{\sigma})\}$$

$$\text{s.t.}\, \sigma_1 > 0,\ \sigma_1 + \mathcal{K}\delta\sigma_{\mathrm{ROI}} > 0$$

with the choice

$$p_{\bar{\sigma}}(\bar{\sigma}) = \|L_{\sigma}(\sigma_1 - \sigma^*)\|^2 + \alpha\mathrm{TV}(\delta\sigma_{\mathrm{ROI}}),$$

where $\alpha > 0$ is a weighting parameter. Further,

$$\mathrm{TV}(\sigma) = \sum_{k=1}^{N_e} |e_k|\sqrt{\|(\nabla\sigma)|_{e_k}\|^2 + \beta}$$

is a differentiable approximation of the isotropic TV functional [90], $(\nabla\sigma)|_{e_k}$ is the (constant) gradient of the (piecewise linear) σ at element e_k, and N_e is the number of elements in the mesh that is used for the representation of σ. $\beta > 0$ is a small parameter which ensures that $\mathrm{TV}(\sigma)$ is differentiable.

(E5) Estimate of $\bar{\sigma} = (\sigma_1^{\mathrm{T}}, \delta\sigma^{\mathrm{T}})^{\mathrm{T}}$ with the **non-linear difference reconstruction** in the case where $\Omega_{\mathrm{ROI}} = \Omega$. That is, estimate (E5) provides a non-linear difference reconstruction in a case where no ROI constraints are used. Here, $p_{\bar{\sigma}}(\bar{\sigma})$ is chosen as in (E4), except for the difference in the selection of ROI.

In each test case, the sub-domain Ω_{ROI} in estimates (E3) and (E4) is the same. The minimization problems in (E1), (E4) and (E5) are solved by using the Gauss-Newton method with a line search. The positivity constraint on the conductivity is handled by using interior point methods [80,81].

4.2 PUBLICATION I: ESTIMATION OF CONDUCTIVITY CHANGES IN A REGION OF INTEREST WITH EIT

The motivation of the studies in Publication **I** originated from a potential new application of EIT: glottal imaging (see Section 3.2). In glottal imaging, the goal is to monitor physiological changes in glottal due to the closing and opening of the glottis. A nice property of the glottal imaging in EIT is the possibility of carrying out the reference measurements for difference imaging. We hypothesized that the non-linear difference imaging approach could improve the quality of the reconstructions, especially if the location of the change in the target is relatively well known inside the body. The approach was tested both experimentally and with a 2D simulation corresponding to a neck shaped geometry.

4.2.1 Measurement configuration

The measurements were conducted using a cylindrical tank shown in the top row of Figure 4.1. The diameter of the tank was 28 cm.

Sixteen equally spaced metallic electrodes (width 2.5 cm, height 7.0 cm) were attached to the inner surface of the tank. In Figure 4.1, the electrode locations are indicated with brown stripes on the tank wall. The rightmost electrode was identified with electrode index $\ell = 1$, and the electrode indices increased in counter clockwise direction. The tank was filled with saline. In the initial state σ_1, a plastic bar was placed in the tank to form an inhomogeneous background. In the second state σ_2, a plastic triangular prism was added to the tank to form a conductivity change. Pairwise current injections were applied in the measurements. The currents were injected in such a way that one electrode was fixed as the sink electrode and then pairwise currents were sequentially applied between the sink electrode and each one of the 15 remaining electrodes. This process was repeated using electrodes $\{1, 5, 9, 13\}$ as the sink, leading to total of 54 current injections when reciprocal current injections were excluded. This will be useful for improving the signal-to-noise ratio of measurements.

4.2.2 Results

The photographs of the measurement tank at the initial state (conductivity σ_1) and after the change (conductivity σ_2) are shown in the top row of Figure 4.1. The second row shows the estimate (E1) by separate absolute reconstructions. The third and fourth rows show linear reconstructions (E2) and (E3) without and with the ROI constraint, respectively. The estimates (E4) and (E5) with the non-linear difference imaging approach are shown in the fifth and sixth row; the fifth row corresponds to the case where the ROI constraint is employed, while in the sixth row case the conductivity change is not restricted to a ROI. In estimates (E4) and (E5), the conductivity after the change is computed from the estimated parameters $(\hat{\sigma}_1, \widehat{\delta\sigma}_{\mathrm{ROI}})$ as $\hat{\sigma}_2 = \hat{\sigma}_1 + \mathcal{K}\widehat{\delta\sigma}_{\mathrm{ROI}}$. In the estimates (E3) and (E4), the boundary of the ROI is indicated by a black line.

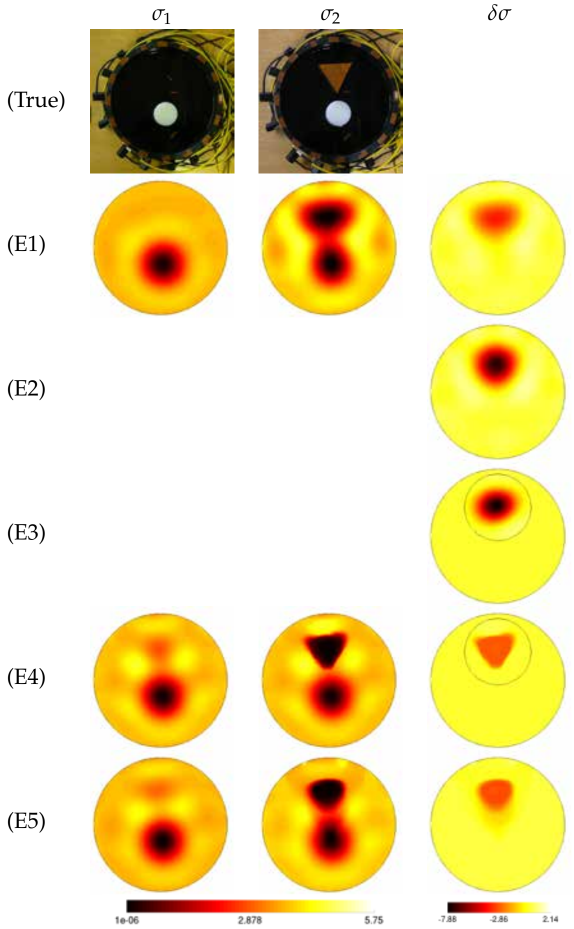

Figure 4.1: Reconstructions from real data. Top row: photographs of the measurement tank. (E1)-(E5) refer to the estimates listed in Section 4.1. (E4) and (E5) are the nonlinear difference reconstructions with and without ROI constraint, respectively.

4.2.3 Discussion

Figure 4.1 shows that all reconstruction methods detect the conductivity change with varying accuracy (estimates for the conductivity change $\delta\sigma$, third column). However, the quality of the estimates (E4) and (E5) obtained with the proposed method is clearly better than the other estimates by visual inspection; especially, in (E4), where the ROI constraint is employed, the triangular shape of the inclusion is recovered notably well.

In Publication **I**, the proposed approach outperformed the frame-by-frame absolute imaging approach and the conventional linear difference imaging approach in all test cases. For example, we considered two cases (refer to Figures 2 & 3 in Publication **I**) to study if the proposed approach can detect the different size of rectangular shaped prisms simulating different glottis opening. The result of this study shows that estimate (E4) was the only estimate capable of differentiating the size, giving the most accurate size estimates for the inclusions (Table 1 in Publication **I**). Further, when the change in $\delta\sigma$ was a thin rectangular shaped prism (Figure 3 in Publication **I**), (E4) shows even the elongated shape of the inclusion, unlike the other estimates.

These findings suggest that the proposed approach could be very useful for difference imaging, especially when the conductivity change is known to occur in some specific ROI inside the body.

In the simulation case of Publication **I** (refer to Figure 4 within), the electrodes were set only on the frontal part of the domain boundary that is close to the ROI where the change of the target was known to take place. The results demonstrated that the proposed approach can tolerate well such a partial boundary setting.

4.3 PUBLICATION II: A NON-LINEAR APPROACH TO DIFFERENCE IMAGING IN EIT: ASSESSMENT OF THE ROBUSTNESS IN THE PRESENCE OF MODELING ERRORS

Since the ability to tolerate modeling errors is one of the main reasons for the wide usage of the linear approach to difference imaging, an interesting question regarding the practical usability of the non-linear approach is: To which extent does it tolerate modeling errors?

In Publication **II**, we studied the robustness of the non-linear difference imaging approach *w.r.t* modeling errors in the forward model of EIT measurements. Modeling errors due to inaccurate knowledge of the boundary shape, truncation of the computational domain, inaccurate knowledge of the contact impedances and electrode positions were considered. The extension of the results of Publication **II** to study the robustness *w.r.t* infeasible choices for regularization functionals is presented in Section 4.3.3.

4.3.1 Measurement configuration & modeling

The experiments were performed using a deformable tank shown in the top row in Figure 4.3. Sixteen identical metallic electrodes (width 2.0 cm and height 7.0 cm) were attached to the inner surface of the tank. The tank was filled with tap water. In the initial state σ_1, a plastic bar was placed in the tank to form an inhomogeneous background. In the state after the change σ_2, a plastic triangular prism was added to the tank to form a conductivity change. The inside circumference of the tank was about 81.5 cm and the geometrical shape of the tank is shown with a black line in Figure 4.2. In the reconstructions, the domain was modeled as a circle (Figure 4.2): this causes a modeling error due to the incorrect knowledge of the boundary shape.

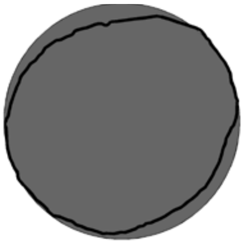

Figure 4.2: Study of the robustness w.r.t mismodeling the boundary shape. Measurement domain Ω ($\partial\Omega$ is shown with solid line) and model domain $\tilde{\Omega}$ shown as gray patch are used for experiment in Section 4.3.1.

4.3.2 Results & Discussion

The results of the robustness study *w.r.t* mismodeling the boundary shape are shown in Figure 4.3, which has the same layout as Figure 4.1. The top row in Figure 4.3 shows the photographs of the measurement tank at the initial state σ_1 and the state after the change σ_2. The estimates (E1)-(E5) are shown in rows 2-6.

Figure 4.3 shows that the estimates $\hat{\sigma}_1$ and $\hat{\sigma}_2$ by the absolute reconstruction (E1) are highly sensitive to the modeling errors, and the estimates contain severe artefacts. However, the change estimate $\widehat{\delta\sigma}$ is relatively feasible, because the artefacts are similar in $\hat{\sigma}_1$ and $\hat{\sigma}_2$, and are partly canceled in the subtraction $\hat{\sigma}_2 - \hat{\sigma}_1$.

The linear difference reconstructions (E2) and (E3) are indicative of the location of the change, but the accuracy of these reconstructions is not very high, and especially the shape of the inclusion is not recovered well. We note that overall in Publication **II** the ROI constrained linear reconstruction (E3) is more sensitive to the modeling errors than the conventional linear difference reconstruction (E2) (see especially Figures 2-4 and 7 in Publication **II**). This is due to the fact that in the ROI constrained case, all the modeling errors, which do not cancel out in the subtraction of the data, are mapped into a smaller dimensional subspace, which represents a subvolume of the body, leading to larger artefacts in the ROI area. Therefore it seems that the use of the ROI constrained linear reconstruction (E3) would not be a robust approach in practical applications.

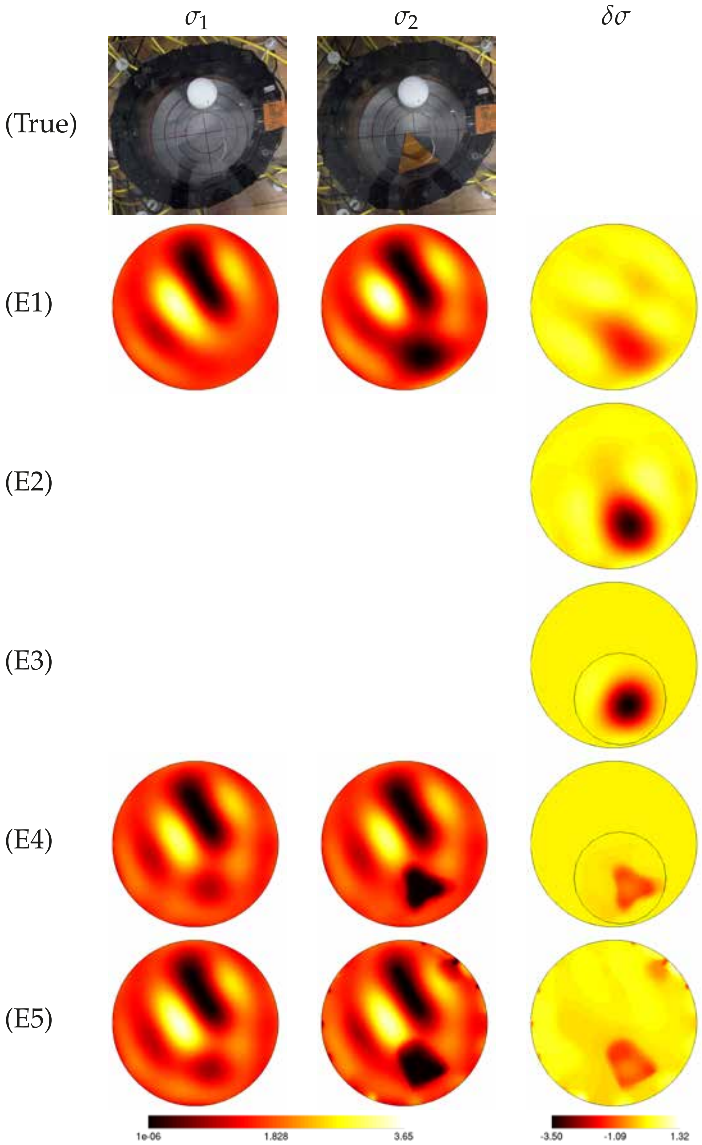

Figure 4.3: Experimental case: Errors due to inaccurately known boundary shape. The measurement set-up and estimates (E1)-(E5) described in Section 4.1 using experimental data. (E4) and (E5) are the non-linear difference reconstructions with and without ROI constraint, respectively.

The estimates (E4) and (E5) with the non-linear difference imaging approach, on the other hand, give qualitatively good reconstructions of the conductivity change $\delta\sigma$. Indeed, although the modeling errors are rather severe, (E4) and (E5) yield conductivity change reconstructions which even show the shape of the inclusion, especially (E4). This implies that the non-linear difference reconstructions, with and without the ROI constraint, tolerate modeling errors well. This finding is also supported quantitatively by the simulation studies with varying level of error in contact impedances (Figure 5 in Publication **II**) and domain modeling errors (Figure 9 in Publication **II**).

Obviously, the reconstructed conductivity distributions $\hat{\sigma}_1$ and $\hat{\sigma}_2$ are heavily affected by the modeling errors also in the estimates (E4) and (E5). The reason for the modeling errors *not* affecting significantly to the estimate $\widehat{\delta\sigma}$ lies in the parameterization of σ_2 as the linear combination of the initial state σ_1 and the change $\delta\sigma$; the modeling errors due to the inaccurate knowledge of auxiliary model parameters are invariant between the times of the measurements $V_1 = U(\sigma_1) + e_1$ and $V_2 = U(\sigma_1 + \mathcal{K}\delta\sigma_{\mathrm{ROI}}) + e_2$. Consequently, when the proposed parametrization is used, the errors caused by the uncertainties in auxiliary model parameters are absorbed by the estimate of σ_1, which consists the parameters that are common for the models of both observations V_1 and V_2.

Overall, the estimates (E4) are more reliable than (E5) – this is evident from the experimental studies in Figure 4.3 in this section and Figure 6 in Publication **II**. This is an expected result, since the prior information on the location of the conductivity change is included in the ROI constrained estimate (E4).

Finally, it is worth noting that in Publication **II** we only studied the robustness of the non-linear difference imaging approach *w.r.t* modeling errors in the forward model of EIT measurements. The effect of misspecifying the regularization functionals in the non-linear difference imaging approach was not thoroughly examined. We note, however, that in the experimental case (Figure 4.3) the regularization functional for σ_1 was infeasible – the true σ_1 contained a very sharp change in the conductivity due to the plastic object in the background, while in the reconstructions a smoothness functional for σ_1 was employed. The robustness of the non-linear difference imaging approach *w.r.t* infeasible choices for regularization functionals is further studied in Section 4.3.3.

The numerical and experimental studies in this publication only considered 2D cases with modeling errors. In reality, however, the targets are always 3D and the target geometry may become complicated. To address this problem, the extensions of the non-linear approach to 3D cases and to more realistic geometries of human body studies in the presence of geometrical modeling errors are studied in Publication **III**.

4.3.3 Assessment of the robustness *w.r.t* infeasible choices for regularization functionals

As an extension of Publication **II**, the effect of misspecifying the regularization functionals for σ_1 and $\delta\sigma_{\mathrm{ROI}}$ to the performance of non-linear difference imaging approach is investigated with simulated EIT data. As discussed in Section 3.1, the two regularization terms $p_{\sigma_1}(\sigma_1)$ and $p_{\delta\sigma_{\mathrm{ROI}}}(\delta\sigma_{\mathrm{ROI}})$ in (3.6) corresponding to conductivity σ_1 and conductivity change $\delta\sigma_{\mathrm{ROI}}$ may have different properties.

In this thesis, we assume that the unknown background σ_1 consists of smoothed objects, and the conductivity change is characterized by a sharp change of the conductivity, representing typical cases in real applications. For example, targets that are results of diffusion processes, are usually modeled with a smoothness functional, while piecewise regular targets which have sharp boundaries might be modeled with a TV functional. Therefore, we select a smoothness functional for $p_{\sigma_1}(\sigma_1)$ and a TV functional for $p_{\delta\sigma_{\mathrm{ROI}}}(\delta\sigma_{\mathrm{ROI}})$. However, in real application, both σ_1 and $\delta\sigma_{\mathrm{ROI}}$ can also be smooth or discontinuous or where σ_1 is discontinuous and $\delta\sigma_{\mathrm{ROI}}$ is smooth.

In order to evaluate the sensitivity of the non-linear difference imaging approach to infeasible choices for regularization functionals, we computed two test cases in Figures 4.4 and 4.5. Figure 4.4 shows the test cases where both the true initial conductivity σ_1 and the true conductivity change $\delta\sigma_{\mathrm{ROI}}$ are smooth, implying that the functional $p_{\delta\sigma_{\mathrm{ROI}}}(\delta\sigma_{\mathrm{ROI}})$ is infeasible in the reconstructions; Figure 4.5 illustrates the test cases where σ_1 is discontinuous and $\delta\sigma_{\mathrm{ROI}}$ is smooth, that is, both regularization functionals $p_{\sigma_1}(\sigma_1)$ and $p_{\delta\sigma_{\mathrm{ROI}}}(\delta\sigma_{\mathrm{ROI}})$ are infeasible. Note that, in both test cases, no modeling errors related to the forward model are present.

Figures 4.4 and 4.5 show that estimates (E1)-(E5) detect the inclusions with varying accuracies. Overall, the quality of (E4) and (E5) obtained with the non-linear approach is clearly better than the other estimates by visual inspection; indeed, the shapes and sizes of the inclusions are recovered notably well in estimates (E4) and (E5).

In summary, the new results in Figures 4.4 and 4.5, together with the experimental case (Figure 4.3) where the regularization functionals were also infeasible, demonstrate that the estimates (E4) and (E5) based on the non-linear difference imaging approach are robust *w.r.t* infeasible choices for regularization functionals.

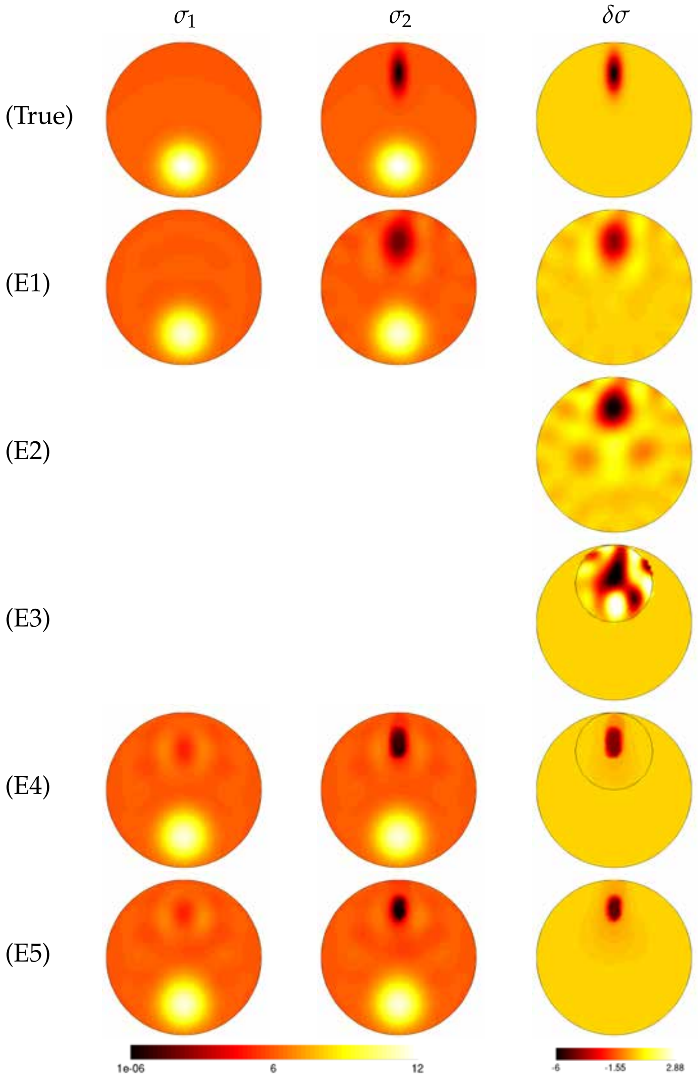

Figure 4.4: Test Case without modeling errors to study the robustness w.r.t infeasible choices for regularization functionals. The true conductivity (top row: both σ_1 and $\delta\sigma$ are smooth) and estimates (E1)-(E5). (E4) and (E5) are the non-linear difference reconstructions with and without ROI constraint, respectively.

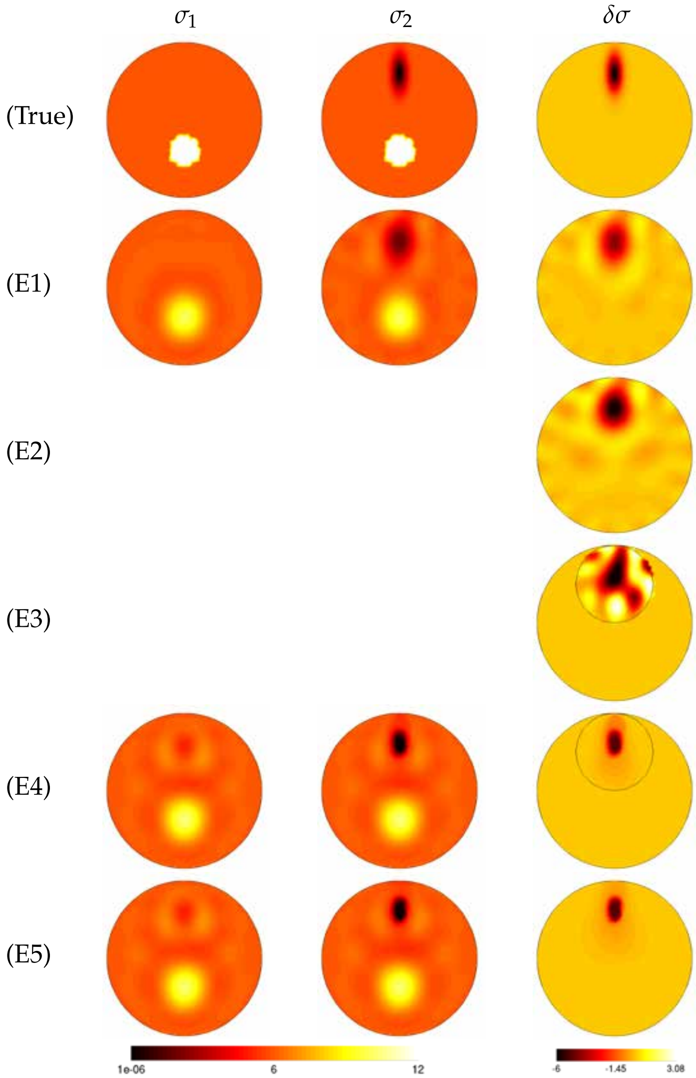

Figure 4.5: Test Case without modeling errors to study the robustness w.r.t infeasible choices for regularization functionals. The true conductivity (top row: σ_1 is discontinuous and $\delta\sigma$ is smooth) and estimates (E1)-(E5). (E4) and (E5) are the non-linear difference reconstructions with and without ROI constraint, respectively.

4.4 PUBLICATION III: NON-LINEAR DIFFERENCE IMAGING APPROACH TO THREE DIMENSIONAL ELECTRICAL IMPEDANCE TOMOGRAPHY IN THE PRESENCE OF GEOMETRIC MODELING ERRORS

In Publication **II**, the non-linear difference imaging approach was found to tolerate a variety of modeling errors in the 2D cases, resulting in better reconstructions of the conductivity change than the linear difference imaging and the approach based on separate absolute reconstructions. In Publication **III**, we investigated how the approach performs in 3D EIT, especially in realistic geometries of human neck and thorax. We evaluated the feasibility of the approach in geometries related to three potential medical applications of EIT: glottal imaging, cardiac imaging and lung imaging, by using simulated data. Two experimental studies with a water tank in the shape and 1:1 scale of a human thorax were also conducted.

4.4.1 Target and model domains

In Publication **III**, the anatomies of the neck and thorax used for the target domains were obtained from computerized tomography images. Because such information in practical situations is often not available, the EIT image reconstruction problems were carried out using approximate model domains.

The meshes for the target domain are shown in Figure 4.6 (left). In the neck model, $L = 32$ disc electrodes with a radius of 0.5 cm were modeled on the boundary $\partial\Omega$. Electrodes 1 through 28 in a 7×4 array were placed on the frontal part of the domain boundary near the glottal area, whereas the other 4 electrodes were horizontally placed on the back side of the domain boundary. In the thorax model, $L = 32$ disc electrodes with a radius of 0.5 cm were arranged in two horizontal rows of sixteen approximately equally spaced electrodes. The locations of electrodes are indicated by red color in Figure 4.6. To study the effect of mismodeling the geometric shape of the target domain, we adapted approximate model domains to solve the image reconstruction problem. As shown in

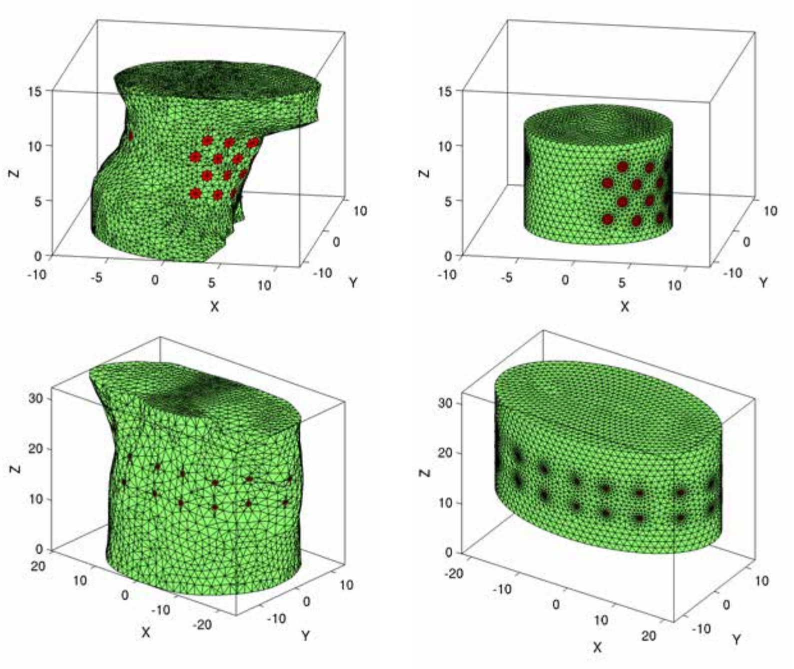

Figure 4.6: Meshes used for numerical studies. Left: meshes of the human neck domain and thorax domain for simulating measurements; Right: meshes of the model domains for the inverse computations.

Figure 4.6 (right), a circular cylinder with radius 6.5 cm and height 9 cm was used for the inverse computations in the simulation study of glottal imaging, while an elliptic cylinder with height 20 cm, semi-major axis 22 cm, and semi-minor axis 13 cm was used for inverse computations in the simulation studies of cardiac and lung imaging. Note that both model domains were also truncated in the z-direction.

4.4.2 Simulation examples

To study the performance of the non-linear difference imaging approach, the following four simulation cases were carried out. In each test case, two measurement sets were simulated: V_1 corresponding to an initial conductivity σ_1 and V_2 corresponding to conductivity σ_2 after the change.

- *Case 1: Glottal imaging with EIT.* In this test case, the initial state σ_1 corresponds to a case where the vocal folds are contacted each other by holding breath, whereas the conductivity after the change σ_2 corresponds to a case where the vocal folds are partially separated, forming a non-conducting strip within the glottis.

- *Case 2: Cardiac imaging with EIT.* Here, the initial state σ_1 presents a heart in the end-systolic phase, whereas the conductivity after the change σ_2 represents the heart in the end-diastolic phase. In the cardiac imaging, one can avoid a significant change of the subject's thorax shape and the conductivity of the lung by asking the subjects to inspire to total lung capacity and to hold their breath for a short measurement time. Therefore, we assume there is no change of the thorax shape and the conductivity of lung during the measurements.

- *Case 3: Lung imaging without a shape change of the thorax.* Here, the initial state σ_1 simulates the thorax in the end-inspiration phase, whereas the conductivity after the change σ_2 simulates the thorax in the end-expiration phase. This case was done to produce an ideal reference case of lung imaging, where the geometric modeling errors between the initial state and the state after the change are assumed to be invariant in the sense that the geometry is the same in both V_1 and V_2.

- *Case 4: Lung imaging with a shape change of the thorax.* In the clinical situations, the thorax shape varies due to breathing and changes with the patient position during the measurements. For this reason, we simulate a more realistic situation lung monitoring, where the shape changes due to breathing, leading to a situation where all the estimates (E1-E5) are more prone to the modeling errors since the (unknown) body geometry in V_1 and V_2 is not the same. The shape change of the thorax is simulated by linear movement and deformation of the front part of the chest, leading to 4.15% change in the volume of the thoracic cavity and 15% change in the lung volume between the initial state and the state after the change, see Fig. 4.7.

Figure 4.7: Study of the lung imaging with a shape change of the thorax in Case 4. Horizontal cross section of the model domain $\hat{\Omega}$ ($\partial\hat{\Omega}$ is shown with solid line) and the target domain Ω is shown as gray patch. Left: thorax at the end-inspiration phase. Middle: thorax at the end-expiration phase. Right: the change of the thorax shape (shown as black patch). When the thorax is in the end-expiration phase, the volume of the thoracic cavity and the size of a lung decrease by 4.15% and 15%, respectively.

4.4.3 Results

The true conductivity distributions at the initial state and after the change and estimates (E1)-(E5) for different test cases are shown in Figures 4.8-4.11. In each of these figures, the top three rows show the horizontal cross sections of the true conductivity distributions and the corresponding estimates; and the bottom three rows show the vertical cross sections of the true conductivity distributions and the corresponding estimates. In Figures 4.8-4.11, the images of the true and estimated conductivity changes $\delta\sigma$ are highlighted with dashed boxes, because the main interest in this study lies in the reconstruction of $\delta\sigma$. In the estimates (E3) and (E4), the boundary of the ROI is indicated by a black line. Again, in estimates (E4) and (E5), the conductivity after the change is computed from the estimated parameters $(\hat{\sigma}_1, \widehat{\delta\sigma}_{\mathrm{ROI}})$ as $\hat{\sigma}_2 = \hat{\sigma}_1 + \mathcal{K}\widehat{\delta\sigma}_{\mathrm{ROI}}$.

To compare the performances of estimates (E1)-(E5), a size coverage ratio (CR) was used to determine how well the sizes of inclusions were recovered. The CR was calculated by dividing the

Table 4.1: The RCRs and the relative contrast value of the reconstructed conductivity change $\delta\sigma$. (E4) and (E5) are the non-linear difference reconstructions with and without ROI constraint.

	Case 1		Case 2		Case 3		Case 4	
	RCR	RCo	RCR	RCo	RCR	RCo	RCR	RCo
(True)	1.00	1.00	1.00	1.00	1.00	1.00	1.00	1.00
(E1)	4.91	1.15	2.17	0.35	0.20	1.96	0.26	1.42
(E2)	1.77	1.31	2.30	0.20	0.39	2.59	0.41	2.06
(E3)	0.32	2.63	1.37	0.37	–	–	–	–
(E4)	0.86	1.12	0.53	1.23	–	–	–	–
(E5)	0.91	1.11	0.53	1.14	0.97	0.98	0.69	0.87

volume of the inclusion by the total volume of the target:

$$\mathrm{CR} = \frac{\text{Inclusion volume}}{\text{Target volume}} \times 100\%.$$

To estimate the volume of the inclusion, we used the half value of the minimum/maximum of the estimates $\widehat{\delta\sigma}$ as the threshold for the inclusion detection. For easy comparison with the true volume, we computed a relative CR (RCR), which was defined as:

$$\mathrm{RCR} = \frac{\mathrm{CR}}{\mathrm{CR}_{\mathrm{True}}}.$$

Further, the maximum/minimum of the reconstructed change was used to measure the accuracy of the recovered contrast. The contrasts of the reconstructed conductivity changes are tabulated in terms of a relative contrast (RCo)

$$\mathrm{RCo} = \frac{\max|\widehat{\delta\sigma}|}{\max|\delta\sigma_{\mathrm{true}}|}.$$

The relative quantities RCR and RCo are used here instead of the respective quantities CR and $\max|\widehat{\delta\sigma}|$ to ease the comparison of the values in Table 4.1. For both RCR and RCo, value 1 would indicate exact match of the true and estimated values of the change.

4.4.4 Discussion

Figure 4.8 illustrates the results of Case 1. In estimate (E1), the subtraction $\hat{\sigma}_2 - \hat{\sigma}_1$ removes the largest artefacts, and consequently the location of the conductivity change is roughly detected. However, severe artefacts are still present in the reconstruction, making it difficult to distinguish between the conductivity change and the artefacts. It is also difficult to assess the shape and size of the conductivity change based on those images. In short, the accuracy of the reconstruction of $\delta\sigma$ is quite poor.

In estimate (E2), the location and shape of the conductivity change are recovered relatively well, and the RCR is already much closer to the true value than (E1), see Table 4.1. However, (E2) overestimates the contrast of $\delta\sigma$ quite heavily. The estimate (E3) is heavily affected by the modeling errors. As noted in Section 4.3.2, this

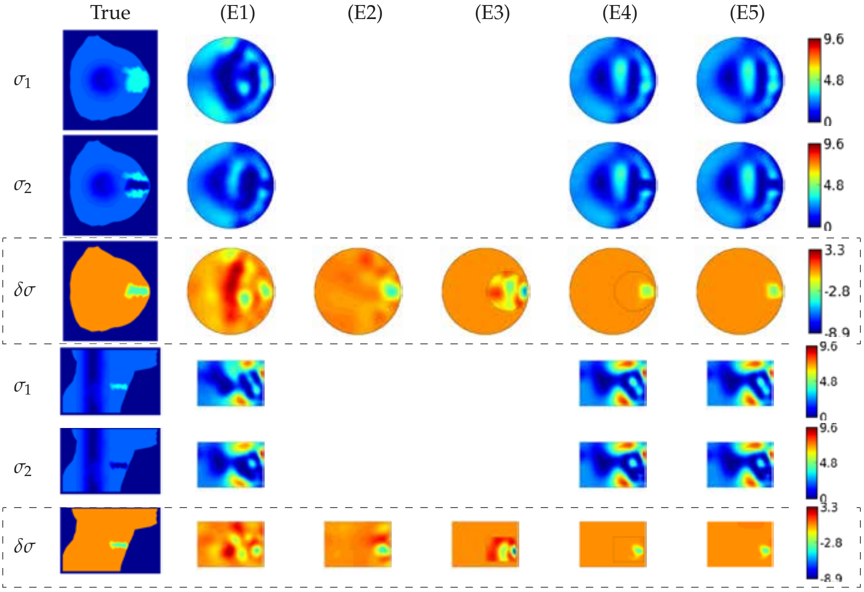

Figure 4.8: Case 1: Horizontal and vertical cross sections of the neck with simulated conductivity distributions and the reconstructions obtained by estimates (E1)-(E5) described in Section 4.1. The dashed boxes highlight the true and estimated conductivity change $\delta\sigma$. (E4) and (E5) are the non-linear difference reconstructions with and without ROI constraint, respectively.

behavior can be explained by the fact that in the ROI constrained linear approach the effects of modeling errors which do not cancel out in the subtraction $V_2 - V_1$, are propagated into a smaller dimensional subspace than in the whole domain estimate (E2), leading to heavy artefacts in the ROI.

The estimates (E4) and (E5) based on the non-linear approach, on the other hand, give the most accurate reconstructions of the conductivity change $\delta\sigma$, e.g. the location and size of the conductivity change are recovered well, as evidenced by the RCR and RCo that are close to the true values, see Table 4.1. It is worth noticing that in (E4) and (E5), the reconstructed conductivity change $\delta\sigma$ is feasible *although* the reconstructed conductivity distributions σ_1 and σ_2 are heavily biased (see Fig. 4.8). As pointed out in Publication **II**, this results from the parametrization used in (E4) and (E5): When modeling errors remain unchanged between states σ_1 and σ_2, the errors caused by the mismodeling are absorbed by the estimate of σ_1,

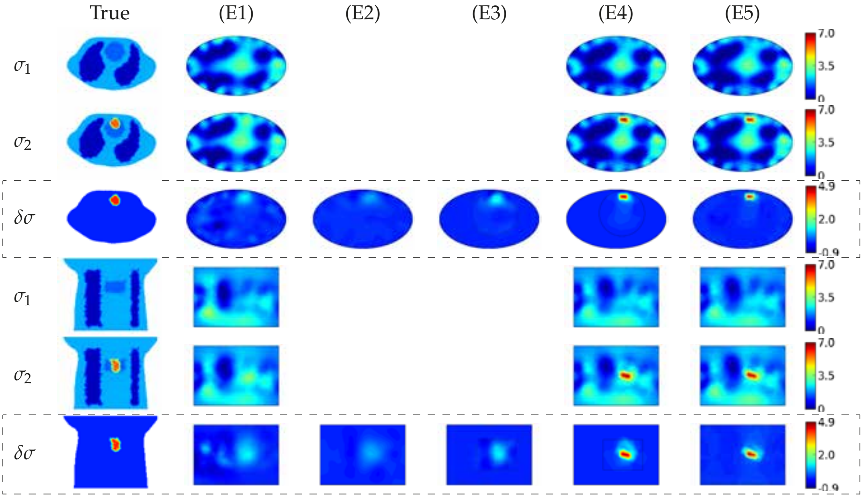

Figure 4.9: Case 2: Horizontal and vertical cross sections at the level of $z = 20$ *cm and* $y = 10$ *cm, respectively. The true conductivity (top row) and the estimates (E1)-(E5) described in Section 4.1. The dashed boxes highlight the true and estimated conductivity change* $\delta\sigma$*. (E4) and (E5) are the non-linear difference reconstructions with and without ROI constraint, respectively.*

which consists of the parameters that are common for the models of both V_1 and V_2.

The results of Case 2 are shown in Figure 4.9. All the estimates detect the conductivity change with varying accuracies. For example, the RCRs are significantly overestimated or underestimated in all the estimates, see Table 4.1. Although the RCRs are underestimated in estimates (E4) and (E5), the quality of the reconstructions with (E4) and (E5) is better than that based on estimates (E1-E3) by visual assessment. This is mainly because the RCos corresponding to (E4) and (E5) are clearly closest to the true values, see Table 4.1.

In the lung imaging (Cases 3 and 4), we only considered the whole domain estimates (E1), (E2) and (E5), since the ROI would cover a significant part the overall volume of the thorax, and in the Case 4, where the thorax deformation between the states is included in the simulation, the selection of the ROI would be somewhat am-

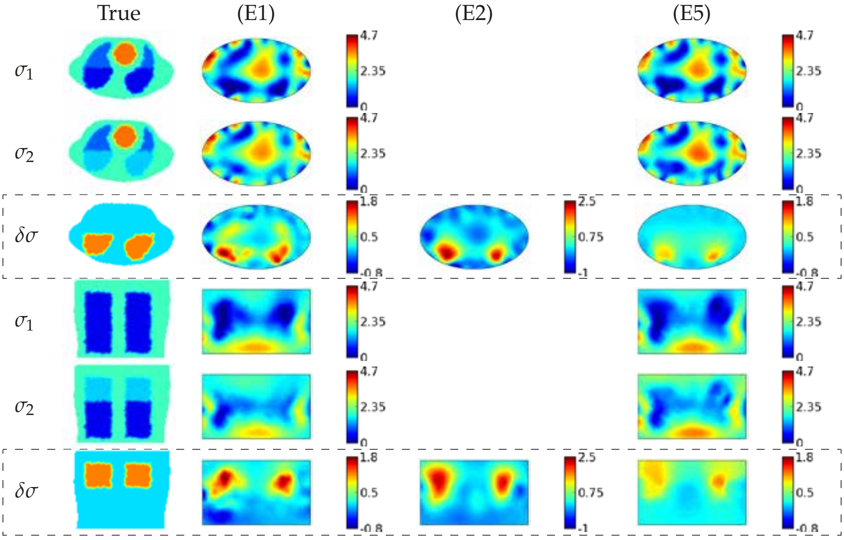

Figure 4.10: Case 3: Lung imaging without a shape change of the thorax. Horizontal and vertical cross sections at the level of $z = 22.5$ cm and $y = -8.5$ cm, respectively. The true conductivity (top row) and the estimates (E1), (E2) and (E5) described in Section 4.1. The dashed boxes highlight the true and estimated conductivity change $\delta\sigma$. (E5) is the non-linear difference reconstructions without ROI constraint.

biguous.

Figure 4.10 shows the results of Case 3 where the thorax shape does not change between the states. Similarly as in Case 1 and Case 2, estimates (E1), (E2) and (E5) detect the conductivity change with varying accuracies. Table 4.1 shows that the RCRs based on (E1) and (E2) are significantly underestimated, and the RCos corresponding to (E1) and (E2) are fairly far from the true values. Estimate (E5), on the other hand, produces the most accurate RCR and RCo, see Table 4.1.

Figure 4.11 shows the results of Case 4. As expected, the reconstructed conductivity changes in all the estimates are worse compared to Case 3, due to the change of the thorax shape between the states σ_1 and σ_2. However, the performance of the approaches compared to each other remains similar to the more ideal case 3; the estimate (E5) gives again quantitatively most accurate reconstruction of the conductivity change.

In overall, the results of the simulated test cases indicate that the non-linear approach improves the accuracy of the estimates of

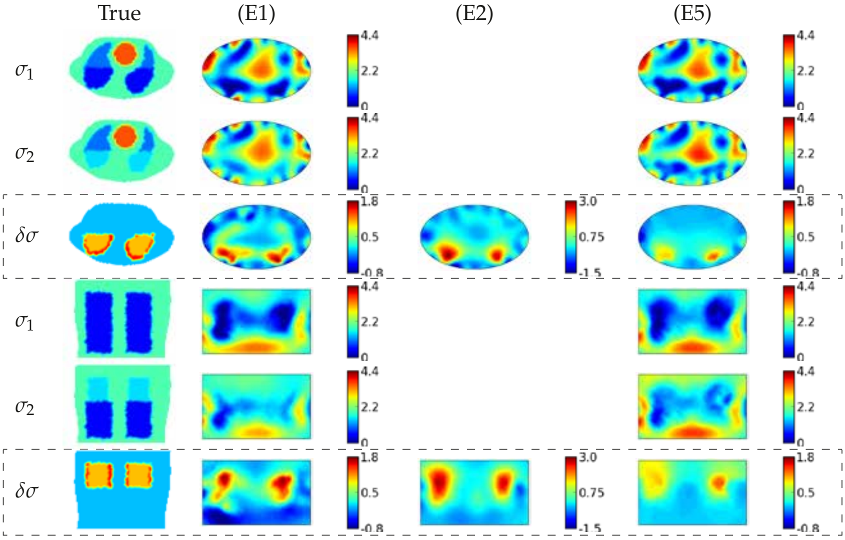

Figure 4.11: Case 4: Lung imaging with a change of the thorax shape, otherwise as in Figure 4.10.

$\delta\sigma$ compared to the approaches based on separate absolute reconstructions and the linear approach to difference imaging, and that the approach tolerates 3D geometrical modeling errors at least to the same extent as the linear approach. The result of Case 4 indicates that this also extends to the cases where the modeling errors are variant between the states. This is a nice feature from the practical point of view, since medical EIT is always accompanied by invariant or variant modeling errors (e.g. geometrical modeling errors) and feasible estimation of the conductivity change plays a very important role in studying activities in organs (e.g. the estimation of conductivity change offers the possibility to study cardiac stroke volume, which is a direct indicator of the cardiac pumping efficiency [82,83]).

5 Summary and conclusions

In this thesis, a non-linear difference imaging approach was developed for EIT. In the proposed approach, the conductivity after the change is parameterized as a linear combination of the (unknown) initial conductivity and the conductivity change. The approach is based on regularized non-linear LS framework. The EIT measurements taken before and after the change are concatenated into a single measurement vector, and the inverse problem is to simultaneously reconstruct the initial conductivity and the conductivity change based on the combined data. This approach allows independently modeling the spatial characteristics of the initial conductivity and the change by applying different regularization functionals, and it also allows for the restriction of the conductivity change to a ROI in cases where the changes are *a priori* known to occur in a certain subvolume of the body.

In Publication **I**, the proposed approach was tested with three test cases using experimental data and one simulated test case related to a potential new application of EIT: glottal imaging. The proposed approach outperformed the frame-by-frame absolute imaging approach and the conventional linear difference imaging approach in all test cases. Those findings suggest that the proposed approach can be useful in EIT applications where one is interested in detecting the conductivity change between two time instants, especially when the conductivity change is known to be restricted to a relatively small sub-domain. The results of the simulation study demonstrated that the proposed approach can be particularly beneficial in partial boundary data problems. Furthermore, this finding suggests that one could employ existing multichannel electroglottography measurement geometry [53] for glottal imaging with EIT and therefore the proposed approach could allow flexibility in design of a practical measurement system.

In Publication **II**, the performance of the non-linear difference imaging approach in 2D EIT in the presence of modeling errors was studied. Modeling errors related to domain truncation, inaccurately known electrode locations, unknown contact impedances and inaccurately known domain boundary were studied. The approach was evaluated both with numerical simulations and with experiments. The non-linear difference imaging approach was compared with the approach based on separate absolute reconstructions and linear difference imaging. The non-linear difference imaging was shown to produce better estimates for the conductivity change than the conventional approaches, and it was found to tolerate modeling errors at least to the same extent as the linear difference imaging. Furthermore, in the extension of Publication **II**, it was found that the non-linear approach is also in some extent tolerant to infeasible choices for regularization functionals, giving better estimate of the conductivity change than the conventional approaches. These findings suggest that the non-linear approach is well suited to difference imaging in EIT, can handle well challenges of involving modeling errors, unknown initial state and high contrast changes.

In Publication **III**, the non-linear difference imaging approach was applied to 3D EIT in the presence of geometric modeling errors. The feasibility of the non-linear approach was evaluated with simulated examples of glottal imaging, cardiac imaging and lung imaging in EIT, and with phantom measurements. The performance of the non-linear approach was compared to the approaches based on separate absolute reconstructions and the linear difference reconstruction. The study demonstrated that in realistic 3D geometries the non-linear approach tolerates 3D geometrical modeling errors at least to the same extent as the linear approach to difference imaging, and provides quantitative information on the conductivity change.

In many practical EIT applications the reconstruction problems are always accompanied by modeling errors. The modeling errors pose a considerable difficulty in making absolute imaging as a practical EIT reconstruction method since it is well known that even slight mismodeling can quite easily ruin the reconstruction of the conductivity. Thus there is a great need for reliable reconstructions that tolerate modeling errors and give quantitative information. The linear approach to difference imaging is a widely used reconstruction method in EIT, due to the ability to tolerate modeling errors in some extent. However, the linear approach only produces qualitative information and it may be insufficient for the detection of the clinically relevant high contrast changes. These limitations in the reconstruction method are partly responsible for the relatively low use of EIT in clinics. The non-linear approach developed in this thesis handles well challenges involving high contrast changes, unknown initial state and modeling errors.

In conclusion, the non-linear difference imaging approach was demonstrated to produce better estimates of the conductivity change than the conventional approaches and it was found to tolerate modeling errors at least to the same extent as the conventional linear approach to difference imaging. Thus, it seems that the difference imaging with the non-linear approach might be a feasible choice for difference EIT reconstruction method in the clinical use.

Bibliography

[1] K. S. Cheng, D. Isaacson, J. C. Newell, and D. G. Gisser, "Electrode models for electric current computed tomography," *Biomedical Engineering, IEEE Transactions on* **36,** 918–924 (1989).

[2] M. Cheney, D. Isaacson, and J. C. Newell, "Electrical Impedance Tomography," *SIAM Review* **41,** 85–101 (1999).

[3] B. Brown, "Electrical impedance tomography (EIT): a review," *Journal of Medical Engineering & Technology* **27,** 97–108 (2003).

[4] W. Daily, A. Ramirez, D. LaBrecque, and J. Nitano, "Electrical resistivity tomography of vadose water movement," *Water. Resour. Res.* **28,** 1429–1442 (1992).

[5] M. Loke and R. Barker, "Practical techniques for 3D resistivity surveys and data inversion," *Geophysical prospecting* **44,** 499–523 (1996).

[6] P. David, T. Panagiotis, and A. Konstantinos, "Electrical resistivity tomography mapping of beachrocks: application to the island of Thassos (N. Greece)," *Environmental Earth Sciences* **59,** 233–240 (2009).

[7] S. Passaro, "Marine electrical resistivity tomography for shipwreck detection in very shallow water: a case study from Agropoli (Salerno, southern Italy)," *Journal of Archaeological Science* **37,** 1989–1998 (2010).

[8] D. F. Rucker, G. E. Noonan, and W. J. Greenwood, "Electrical resistivity in support of geological mapping along the Panama Canal," *Engineering Geology* **117,** 121–133 (2011).

[9] G. Bouchette, P. Church, J. E. Mcfee, and A. Adler, "Imaging of compact objects buried in underwater sediments using elec-

trical impedance tomography," *Geoscience and Remote Sensing, IEEE Transactions on* **52,** 1407–1417 (2014).

[10] I. Frerichs, J. Hinz, P. Herrmann, G. Weisser, G. Hahn, T. Dudykevych, M. Quintel, and G. Hellige, "Detection of local lung air content by electrical impedance tomography compared with electron beam CT," *Journal of applied physiology* **93,** 660–666 (2002).

[11] V. Cherepenin, A. Karpov, A. Korjenevsky, V. Kornienko, Y. Kultiasov, M. Ochapkin, O. V. Trochanova, and J. D. Meister, "Three-dimensional EIT imaging of breast tissues: System design and clinical testing," *IEEE Trans. Med. Imag* **21,** 662–667 (2002).

[12] Y. Zou and Z. Guo, "A review of electrical impedance techniques for breast cancer detection," *Medical engineering & physics* **25,** 79–90 (2003).

[13] G. Boverman, T. J. Kao, R. Kulkarni, B. S. Kim, D. Isaacson, G. J. Saulnier, and J. C. Newell, "Robust linearized image reconstruction for multifrequency EIT of the breast," *Medical Imaging, IEEE Transactions on* **27,** 1439–1448 (2008).

[14] T. Tidswell, A. Gibson, R. H. Bayford, and D. S. Holder, "Three-dimensional electrical impedance tomography of human brain activity," *NeuroImage* **13,** 283–294 (2001).

[15] A. P. Bagshaw, A. D. Liston, R. H. Bayford, A. Tizzard, A. P. Gibson, A. T. Tidswell, M. K. Sparkes, H. Dehghani, C. D. Binnie, and D. S. Holder, "Electrical impedance tomography of human brain function using reconstruction algorithms based on the finite element method," *Neuroimage* **20,** 752–764 (2003).

[16] D. Scott and H. McCann, eds., *Handbook of Process Imaging for Automatic Control* (CRC Press, 2005).

[17] A. Lipponen, A. Seppänen, and J. Kaipio, "Nonstationary approximation error approach to imaging of three-dimensional

pipe flow: experimental evaluation," *Measurement Science and Technology* **22,** 104013 (2011).

[18] D. Liu, A. K. Khambampati, S. Kim, and K. Y. Kim, "Multiphase flow monitoring with electrical impedance tomography using level set based method," *Nuclear Engineering and Design* **289,** 108–116 (2015).

[19] T. Hou, K. Loh, and J. Lynch, "Spatial conductivity mapping of carbon nanotube composite thin films by electrical impedance tomography for sensing applications," *Nanotechnology* **18** (2007).

[20] T. Hou and J. Lynch, "Electrical impedance tomographic methods for sensing strain fields and crack damage in cementitious structures," *J. Intel. Mat. Syst. Str.* **20,** 1363–1379 (2009).

[21] K. Karhunen, A. Seppänen, A. Lehikoinen, P. Monteiro, and J. Kaipio, "Electrical Resistance Tomography imaging of concrete," *Cement Concrete Res.* **40,** 137–145 (2010).

[22] K. Karhunen, A. Seppänen, A. Lehikoinen, J. Blunt, J. Kaipio, and J. Monteiro, "Electrical Resistance Tomography For Assessment Of Cracks In Concrete," *ACI mater. J.* **107,** 523–531 (2010).

[23] M. Hallaji, A. Seppänen, and M. Pour-Ghaz, "Electrical impedance tomography-based sensing skin for quantitative imaging of damage in concrete," *Smart Materials and Structures* **23,** 085001 (2014).

[24] M. Hallaji, A. Seppänen, and M. Pour-Ghaz, "Electrical resistance tomography to monitor unsaturated moisture flow in cementitious materials," *Cement and Concrete Research* **69,** 10–18 (2015).

[25] J. P. Kaipio, V. Kolehmainen, E. Somersalo, and M. Vauhkonen, "Statistical inversion and Monte Carlo sampling methods

in electrical impedance tomography," *Inverse problems* **16,** 1487 (2000).

[26] D. S. Holder, "Electrical Impedance Tomography: Methods, History and Applications," *Medical Physics* **32,** 2731 (2005).

[27] J. Mueller and S. Siltanen, *Linear and Nonlinear Inverse Problems with Practical Applications* (SIAM, 2012).

[28] P. Vauhkonen, M. Vauhkonen, T. Savolainen, and J. Kaipio, "Three-dimensional electrical impedance tomography based on the complete electrode model," *IEEE Trans. Biomed. Eng* **46,** 1150–1160 (1999).

[29] D. Barber and B. Brown, "Applied potential tomography," *Journal of physics. E. Scientific instruments* **17,** 723–733 (1984).

[30] D. Barber and B. Brown, "Recent developments in applied potential tomography-APT," in *Information processing in medical imaging* (Springer, 1986), pp. 106–121.

[31] D. Barber and A. Seagar, "Fast reconstruction of resistance images," *Clinical Physics and Physiological Measurement* **8,** 47 (1987).

[32] M. Cheney, D. Isaacson, J. Newell, S. Simske, and J. Goble, "NOSER: An algorithm for solving the inverse conductivity problem," *International Journal of Imaging Systems and Technology* **2,** 66–75 (1990).

[33] R. Smallwood, A. Hampshire, B. Brown, R. Primhak, S. Marven, and P. Nopp, "A comparison of neonatal and adult lung impedances derived from EIT images," *Physiological measurement* **20,** 401 (1999).

[34] R. Blue, D. Isaacson, and J. Newell, "Real-time three-dimensional electrical impedance imaging," *Physiological measurement* **21,** 15 (2000).

[35] A. Adler, R. Guardo, and Y. Berthiaume, "Impedance imaging of lung ventilation: do we need to account for chest expansion?," *Biomedical Engineering, IEEE Transactions on* **43,** 414–420 (1996).

[36] V. Kolehmainen, M. Vauhkonen, P. Karjalainen, and J. Kaipio, "Assessment of errors in static electrical impedance tomography with adjacent and trigonometric current patterns," *Physiological measurement* **18,** 289 (1997).

[37] I. Frerichs, "Electrical impedance tomography (EIT) in applications related to lung and ventilation: a review of experimental and clinical activities," *Physiological measurement* **21,** R1 (2000).

[38] B. Harrach and J. K. Seo, "Detecting inclusions in electrical impedance tomography without reference measurements," *SIAM Journal on Applied Mathematics* **69,** 1662–1681 (2009).

[39] M. K. Choi, B. Harrach, and J. K. Seo, "Regularizing a linearized EIT reconstruction method using a sensitivity-based factorization method," *Inverse Problems in Science and Engineering* **22,** 1029–1044 (2014).

[40] M. Soleimani, C. Gómez-Laberge, and A. Adler, "Imaging of conductivity changes and electrode movement in EIT," *Physiological measurement* **27,** S103 (2006).

[41] A. Boyle and A. Adler, "The impact of electrode area, contact impedance and boundary shape on EIT images," *Physiological measurement* **32,** 745 (2011).

[42] A. Boyle, A. Adler, and W. R. Lionheart, "Shape deformation in two-dimensional electrical impedance tomography," *Medical Imaging, IEEE Transactions on* **31,** 2185–2193 (2012).

[43] D. Holder and A. Khan, "Use of polyacrylamide gels in a saline-filled tank to determine the linearity of the Sheffield

Mark 1 electrical impedance tomography (EIT) system in measuring impedance disturbances," *Physiological measurement* **15,** A45 (1994).

[44] G. Hahn, A. Just, T. Dudykevych, I. Frerichs, J. Hinz, M. Quintel, and G. Hellige, "Imaging pathologic pulmonary air and fluid accumulation by functional and absolute EIT," *Physiological measurement* **27,** S187 (2006).

[45] J. Snyder, Y. Silverman, Y. Bai, and M. A. MacIver, "Underwater object tracking using electrical impedance tomography," in *Intelligent Robots and Systems (IROS), 2012 IEEE/RSJ International Conference on* (IEEE, 2012), pp. 520–525.

[46] J. A. Victorino, J. B. Borges, V. N. Okamoto, G. F. Matos, M. R. Tucci, M. P. Caramez, H. Tanaka, F. S. Sipmann, D. C. Santos, C. S. Barbas, et al., "Imbalances in Regional Lung Ventilation A Validation Study on Electrical Impedance Tomography," *American Journal of Respiratory and Critical Care Medicine* **169,** 791–800 (2004).

[47] S. Lindgren, H. Odenstedt, C. Olegård, S. Söndergaard, S. Lundin, and O. Stenqvist, "Regional lung derecruitment after endotracheal suction during volume-or pressure-controlled ventilation: a study using electric impedance tomography," *Intensive care medicine* **33,** 172–180 (2007).

[48] E. L. Costa, R. G. Lima, and M. B. Amato, "Electrical impedance tomography," in *Intensive Care Medicine* (Springer, 2009), pp. 394–404.

[49] S. Leonhardt and B. Lachmann, "Electrical impedance tomography: the holy grail of ventilation and perfusion monitoring?," *Intensive care medicine* **38,** 1917–1929 (2012).

[50] S. Pulletz, A. Adler, M. Kott, G. Elke, B. Gawelczyk, D. Schädler, G. Zick, N. Weiler, and I. Frerichs, "Regional lung opening and closing pressures in patients with acute lung injury," *Journal of Critical Care* **27,** 323–e11 (2012).

[51] S. Zlochiver, D. Freimark, M. Arad, A. Adunsky, and S. Abboud, "Parametric EIT for monitoring cardiac stroke volume," *Physiological measurement* **27,** S139 (2006).

[52] S. Wanjun, Y. Fusheng, Z. Wei, Z. Hongyi, F. Feng, S. Xuetao, L. Ruigang, X. Canhua, D. Xiuzhen, and B. Tingyi, "Image monitoring for an intraperitoneal bleeding model of pigs using electrical impedance tomography," *Physiological Measurement* **29,** 217 (2008).

[53] M. Kob and T. Frauenrath, "A system for parallel measurement of glottis opening and larynx position," *Biomedical Signal Processing and Control* **4,** 221–228 (2009).

[54] A. Seppänen, A. Nissinen, V. Kolehmainen, S. Siltanen, and A. M. Laukkanen, "Electrical impedance tomography imaging of larynx," in *Models and analysis of vocal emissions for biomedical applications, 7th International Workshop* (2011).

[55] D. Liu, A. Seppänen, A. Nissinen, V. Kolehmainen, S. Siltanen, and A. M. Laukkanen, "Preliminary results on 3D electrical impedance tomography imaging of vocal folds," in *8th International Conference on Voice Physiology and Biomechanics* (2012).

[56] T. Hézard, T. Hélie, B. Doval, N. Henrich, and M. Kob, "Non-invasive vocal-folds monitoring using electrical imaging methods," in *100 years of electrical imaging* (2012).

[57] M. Mozumder, T. Tarvainen, A. Seppanen, I. Nissila, S. Arridge, and V. Kolehmainen, "Nonlinear approach to difference imaging in diffuse optical tomography," *Journal of Biomedical Optics* **20,** 105001 (2015).

[58] E. Somersalo, M. Cheney, and D. Isaacson, "Existence and uniqueness for electrode models for electric current computed tomography," *SIAM Journal on Applied Mathematics* **52,** 1023–1040 (1992).

[59] L. M. Heikkinen, T. Vilhunen, R. M. West, and M. Vauhkonen, "Simultaneous reconstruction of electrode contact impedances and internal electrical properties: II. Laboratory experiments," *Measurement Science and Technology* **13,** 1855 (2002).

[60] J. Kaipio and E. Somersalo, *Statistical and Computational Inverse Problems* (Springer New York, 2005).

[61] V. Kolehmainen, *Novel approaches to image reconstruction in diffusion tomography,* PhD thesis (University of Kuopio, Kuopio, Finland, 2001).

[62] L. Borcea, "Electrical impedance tomography," *Inverse problems* **18,** R99–R136 (2002).

[63] P. Vauhkonen, *Image Reconstruction in Three-Dimensional Electrical Impedance Tomography,* PhD thesis (University of Kuopio, Kuopio, Finland, 2004).

[64] V. Kolehmainen, M. Lassas, and P. Ola, "The inverse conductivity problem with an imperfectly known boundary," *SIAM Journal on Applied Mathematics* **66,** 365–383 (2005).

[65] V. Kolehmainen, M. Lassas, and P. Ola, "The inverse conductivity problem with an imperfectly known boundary in three dimensions," *SIAM Journal on Applied Mathematics* **67,** 1440–1452 (2007).

[66] V. Kolehmainen, M. Lassas, P. Ola, S. Siltanen, et al., "Recovering boundary shape and conductivity in electrical impedance tomography," *Inverse Problems and Imaging* **7,** 217–242 (2013).

[67] T. Vilhunen, J. Kaipio, P. Vauhkonen, T. Savolainen, and M. Vauhkonen, "Simultaneous reconstruction of electrode contact impedances and internal electrical properties. Part I: Theory," *Meas. Sci. Technol.* **13,** 1848–1854 (2002).

[68] J. Dardé, N. Hyvönen, A. Seppänen, and S. Staboulis, "Simultaneous reconstruction of outer boundary shape and admit-

tivity distribution in electrical impedance tomography," *SIAM Journal on Imaging Sciences* **6,** 176–198 (2013).

[69] J. Dardé, N. Hyvönen, A. Seppänen, and S. Staboulis, "Simultaneous recovery of admittivity and body shape in electrical impedance tomography: An experimental evaluation," *Inverse Problems* **29,** 085004 (2013).

[70] V. Kolehmainen, M. Lassas, and P. Ola, "Electrical impedance tomography problem with inaccurately known boundary and contact impedances," *Medical Imaging, IEEE Transactions on* **27,** 1404–1414 (2008).

[71] J. Kaipio and E. Somersalo, "Statistical inverse problems: discretization, model reduction and inverse crimes," *Journal of Computational and Applied Mathematics* **198,** 493–504 (2007).

[72] A. Nissinen, L. Heikkinen, V. Kolehmainen, and J. Kaipio, "Compensation of errors due to discretization, domain truncation and unknown contact impedances in electrical impedance tomography," *Meas. Sci. Technol.* **20,** 105504 (13pp) (2009).

[73] A. Nissinen, V. P. Kolehmainen, and J. P. Kaipio, "Compensation of modelling errors due to unknown domain boundary in electrical impedance tomography," *Medical Imaging, IEEE Transactions on* **30,** 231–242 (2011).

[74] A. Nissinen, V. Kolehmainen, and J. P. Kaipio, "Reconstruction of domain boundary and conductivity in electrical impedance tomography using the approximation error approach," *International Journal for Uncertainty Quantification* **1** (2011).

[75] A. I. Nachman, "Global uniqueness for a two-dimensional inverse boundary value problem," *Annals of Mathematics* 71–96 (1996).

[76] S. Siltanen, J. Mueller, and D. Isaacson, "An implementation of the reconstruction algorithm of A. Nachman for the 2-D

inverse conductivity problem," *Inverse Problems* **16,** 681–699 (2000).

[77] K. Knudsen, M. Lassas, J. L. Mueller, and S. Siltanen, "Regularized D-bar method for the inverse conductivity problem," *Inverse Problems and Imaging* **35,** 599 (2009).

[78] E. K. Murphy and J. L. Mueller, "Effect of domain shape modeling and measurement errors on the 2-D D-bar method for EIT," *Medical Imaging, IEEE Transactions on* **28,** 1576–1584 (2009).

[79] M. Vauhkonen, D. Vadasz, J. Kaipio, E. Somersalo, and P. Karjalainen, "Tikhonov regularization and prior information in electrical impedance tomography," *IEEE Trans Med Imaging* **17,** 285–293 (1998).

[80] A. V. Fiacco and G. P. McCormick, *Nonlinear programming: sequential unconstrained minimization techniques* (SIAM, 1990).

[81] J. Nocedal and S. J. Wright, *Numerical optimization*, Vol. 2, (Springer New York, 1999).

[82] A. Vonk-Noordegraaf, A. Janse, J. T. Marcus, J. G. Bronzwaer, P. E. Postmus, T. J. Faes, and P. M. de Vries, "Determination of stroke volume by means of electrical impedance tomography," *Physiological measurement* **21,** 285 (2000).

[83] S. Zlochiver, D. Freimark, M. Arad, A. Adunsky, and S. Abboud, "Parametric EIT for monitoring cardiac stroke volume," *Physiological measurement* **27,** S139 (2006).

[84] T. Dai, C. Gómez-Laberge, and A. Adler, "Reconstruction of conductivity changes and electrode movements based on EIT temporal sequences," *Physiological measurement* **29,** S77 (2008).

[85] T. N. Tallman, S. Gungor, K. W. Wang, and C. E. Bakis, "Damage detection and conductivity evolution in carbon nanofiber epoxy via electrical impedance tomography," *Smart Materials and Structures* **23,** 045034 (2014).

[86] D. Liu, V. Kolehmainen, S. Siltanen, A. M. Laukkanen, and A. Seppänen, "Estimation of conductivity changes in a region of interest with electrical impedance tomography," *Inverse Problems and Imaging* **9,** 211–229 (2015).

[87] L. Slater, A. Binley, W. Daily, and R. Johnson, "Cross-hole electrical imaging of a controlled saline tracer injection," *Journal of applied geophysics* **44,** 85–102 (2000).

[88] A. Kemna, B. Kulessa, and H. Vereecken, "Imaging and characterisation of subsurface solute transport using electrical resistivity tomography (ERT) and equivalent transport models," *Journal of Hydrology* **267,** 125–146 (2002).

[89] C. Lieberman, K. Willcox, and O. Ghattas, "Parameter and state model reduction for large-scale statistical inverse problems," *SIAM Journal on Scientific Computing* **32,** 2523–2542 (2010).

[90] L. I. Rudin, S. Osher, and E. Fatemi, "Nonlinear total variation based noise removal algorithms," *Physica D: Nonlinear Phenomena* **60,** 259–268 (1992).

Dong Liu

Non-linear Difference Imaging Approach to Electrical Impedance Tomography

Electrical impedance tomography (EIT) is an imaging modality in which the conductivity distribution of a body is reconstructed from electrical boundary measurements. Reconstructing the conductivity distribution based on EIT measurements is an ill-posed inverse problem and thus highly intolerant to modeling errors (such as inaccuracy of the body shape). In this thesis, a novel non-linear difference imaging approach is proposed. The numerical and experimental results demonstrate that non-linear difference imaging is relatively tolerant to several modeling errors and provide quantitative reconstructions of the conductivity change in 2D and 3D EIT.

UNIVERSITY OF
EASTERN FINLAND

Publications of the University of Eastern Finland
Dissertations in Forestry and Natural Sciences

ISBN: 978-952-61-1994-6 (PRINTED)
ISBN: 978-952-61-1995-3 (PDF)
ISSN: 1798-5668
ISSN: 1798-5676 (PDF)